Monthly Notices
of the
ROYAL ASTRONOMICAL SOCIETY

MNRAS **458,** 4297–4320 (2016)
Advance Access publication 2016 March 11

doi:10.1093/mnras/stw577

Tracing black hole accretion with SED decomposition and IR lines: from local galaxies to the high-z Universe

C. Gruppioni,[1⋆] S. Berta,[2] L. Spinoglio,[3] M. Pereira-Santaella,[4] F. Pozzi,[5] P. Andreani,[6] M. Bonato,[7] G. De Zotti,[8] M. Malkan,[9] M. Negrello,[10] L. Vallini[1,5] and C. Vignali[5]

[1]*Istituto Nazionale di Astrofisica - Osservatorio Astronomico di Bologna, via Ranzani 1, I-40127 Bologna, Italy*
[2]*Max-Planck-Institut für Extraterrestrische Physik (MPE), Postfach 1312, D-85741 Garching, Germany*
[3]*Istituto Nazionale di Astrofisica - Istituto di Astrofisica e Planetologia Spaziali, via Fosso del Cavaliere 100, I-00133 Roma, Italy*
[4]*Centro de Astrobiologìa (CSIC/INTA), Ctra de Torrejòn a Ajalvir, km 4, E-28850 Torrejòn de Ardoz, Madrid, Spain*
[5]*Dipartimento di Fisica e Astronomia, Università di Bologna, viale Berti Pichat 6, I-40127 Bologna, Italy*
[6]*European Southern Observatory, Karl-Schwarzschild-Straße 2, D-85748 Garching, Germany*
[7]*Department of Physics and Astronomy, Tufts University, 574 Boston Ave, Medford, MA 02155, USA*
[8]*Istituto Nazionale di Astrofisica - Osservatorio Astronomico di Padova, vicolo del'Osservatorio 5, I-35122 Padova, Italy*
[9]*Department of Physics and Astronomy, UCLA, Los Angeles, CA 90095-1547, USA*
[10]*School of Physics and Astronomy, Cardiff University, Queen's Buildings, The Parade, Cardiff CF24 3AA, UK*

Accepted 2016 March 7. Received 2016 March 4; in original form 2015 November 30

ABSTRACT

We present new estimates of AGN accretion and star formation (SF) luminosity in galaxies obtained for the local 12 μm sample of Seyfert galaxies (12MGS), by performing a detailed broad-band spectral energy distribution (SED) decomposition including the emission of stars, dust heated by SF and a possible AGN dusty torus. Thanks to the availability of data from the X-rays to the sub-millimetre, we constrain and test the contribution of the stellar, AGN and SF components to the SEDs. The availability of *Spitzer*-InfraRed Spectrograph (IRS) low-resolution mid-infrared (mid-IR) spectra is crucial to constrain the dusty torus component at its peak wavelengths. The results of SED fitting are also tested against the available information in other bands: the reconstructed AGN bolometric luminosity is compared to those derived from X-rays and from the high excitation IR lines tracing AGN activity like [Ne V] and [O IV]. The IR luminosity due to SF and the intrinsic AGN bolometric luminosity are shown to be strongly related to the IR line luminosity. Variations of these relations with different AGN fractions are investigated, showing that the relation dispersions are mainly due to different AGN relative contribution within the galaxy. Extrapolating these local relations between line and SF or AGN luminosities to higher redshifts, by means of recent *Herschel* galaxy evolution results, we then obtain mid- and far-IR line luminosity functions useful to estimate how many star-forming galaxies and AGN we expect to detect in the different lines at different redshifts and luminosities with future IR facilities (e.g. *JWST, SPICA*).

Key words: galaxies: active – galaxies: evolution – galaxies: Seyfert – galaxies: star formation – infrared: galaxies.

1 INTRODUCTION

The comoving rates of star formation (SF) and central black hole accretion follow a similar rise and fall, offering evidence for co-evolution of black holes and their host galaxies (i.e. Shankar, Weinberg & Miralda-Escudé 2009; Kormendy & Ho 2013 and references therein). The data show that the SF activity peaked at around 8–11 Gyr ago (at redshifts between 1 and 3; e.g. Burgarella et al. 2013). In this phase most of the energy emitted in the SF process was absorbed by dust and converted into infrared (IR), with less than 10 per cent remaining visible at ultraviolet (UV) to optical wavelengths (e.g. Madau & Dickinson 2014). While the large majority of present-day stars have been produced in such obscured galaxies, we have very limited knowledge about the nature of IR galaxies at those high redshifts, on what controlled and changed the SF along the evolution of these galaxies and of their metal content at early epochs. Dusty galaxies are the only ones that can tell us the whole

⋆ E-mail: carlotta.gruppioni@oabo.inaf.it

story of galaxy and AGN evolution (whose activity peaks at about the same epoch) during that obscured era. So far, mid- and far-IR facilities like *ISO*, *Spitzer* and – more recently – *Herschel* have allowed us to observe the 'obscured' side of the Universe at non-local redshifts mostly in photometry, by measuring total fluxes of galaxies, but not peering into their internal physics. This could be done through mid- and far-IR spectroscopic observations, only for local galaxies or, at high redshifts, for few lensed and/or ultraluminous sources not representative of the bulk of the galaxy population.

Emission-line intensities and emission-line ratios in the mid- and far-IR domain, not suffering from dust extinction as the optical and UV emission lines, provide unique information on the physical conditions (i.e. electron density and temperature, degree of ionization and excitation, chemical composition) of the gas responsible for emitting the lines within the dust-obscured regions of galaxies with intense SF activity or surrounding an AGN (Spinoglio & Malkan 1992; Rubin et al. 1994; Panuzzo et al. 2003). The typical electron density of the emitting gas can be identified through IR fine-structure lines, since different IR fine-structure transitions of the same ion have different critical density to collisional de-excitation (e.g. [O III] at 52 and 88 μm). Moreover, the relative strengths of the fine-structure lines in different ionization stages can probe the primary spectrum of the ionizing source, with these line ratios providing information on the age of the ionizing stellar population and on the ionization parameter in single H II regions or in starbursts of short duration. In addition, these line ratios are sensitive to the presence of non-stellar sources of ionizing photons, like the AGN, with some of these lines with higher ionization potential ([Ne V] at 14.32 and 24.32 μm, and [O IV] at 25.89 μm) excited only – or primarily – by an AGN (Genzel et al. 1998; Armus et al. 2007).

In the analysis performed in this work, we have considered the two polycyclic aromatic hydrocarbon (PAH) features at 6.2 and 11.25 μm and several mid- and far-IR fine-structure lines, including four emission lines from photodissociation regions, PDRs ([Si II] 34.8 μm, [O I] 63 μm, [O I] 145.5 μm and [C II] 157.7 μm), seven stellar/H II region lines ([Ne II] 12.8 μm, [S III] 18.7 μm, [S III] 33.5 μm, [O III] 51.8 μm, [N III] 57.3 μm, [O III] 88 μm and [N II] 122 μm) and four AGN lines ([Ne V] at 14.3 and 24.3 μm, [Ne III] 15.5 μm and [O IV] 25.9 μm).

In Spinoglio et al. (2012) 'global' relations between the luminosity of the above lines and the total IR luminosity were derived for all the sources of the 12-μm-selected sample of Seyfert galaxies (12MGS; Rush, Malkan & Spinoglio 1993), regardless the AGN type and the fraction of AGN contributing to the IR luminosity, while in Bonato et al. (2014b) an attempt was made to correlate the line luminosity with the SF IR luminosity and the AGN bolometric luminosity, although the latter was derived using just a few representative spectral energy distribution (SED) templates, normalized to the observed 12 μm flux density.

What is new in our approach with respect to the previous works is that we use the broad-band photometry, from UV to millimetre (mm), to constrain the stellar and SF components, and the *Spitzer*-IRS spectra to constrain the torus. Moreover, we derive new relations between the line and the total IR/AGN accretion luminosities by accounting for the different AGN contributions, finding different relations for AGN dominated sources with respect to SF dominated ones.

The total IR, SF and AGN bolometric luminosities have been derived by performing a detailed three-components (emission from stars, dust heated by SF and a possible AGN dusty torus) SED decomposition (Berta et al. 2013) of the well-studied and extensively observed 12MGS local sample. We note that, thanks to the very detailed data (IR spectrum and photometry along the whole SED), available for this local sample, we are able to constrain the crucial physical quantities characterizing the AGN and its host galaxy like, i.e. star-formation rate (SFR), AGN luminosity, stellar mass and AGN fraction. On the contrary, similar works performed on higher-z samples cannot reach the same kind of precision on the physical parameter derivation, because the constraints are not as many, as good and as detailed as here.

The resulting SF and the reconstructed AGN bolometric luminosities are then related to the available mid- and far-IR line luminosities and used to derive new estimates of the relationships between the luminosity of PAH features and fine-structure lines and AGN bolometric or SF luminosity. Variations of these relations with different AGN fractions are investigated. By extrapolating these local line versus AGN (or SF) luminosity relations to higher redshifts, by means of recent *Herschel* galaxy evolution results (e.g. Gruppioni et al. 2013), we then obtain mid- and far-IR line luminosity functions (LFs). Thanks to the line LFs we can then estimate how many SF galaxies and AGNs we expect to detect in the different IR lines at different redshifts with future IR facilities, like, e.g. the *James Webb Space Telescope* (*JWST*; Gardner et al. 2006) and the *SPace IR telescope for Cosmology and Astrophysics* (*SPICA*; Nakagawa, Matsuhara & Kawakatsu 2012).

The paper is organized as follows. We present the 12MGS Seyfert sample in Section 2. In Sections 3 and 4, we present the SED decomposition method and discuss the main results obtained. In Sections 5 and 6, we derive the AGN/SB diagnostics and the relations between the line and the SF or accretion luminosity. In Section 7, we derive the line LFs up to high redshifts and the estimates for future IR facilities. Finally, in Section 8 we present our conclusions.

Throughout this paper, we use a Chabrier (2003) initial mass function (IMF) and we adopt a ΛCDM cosmology with $H_0 = 71\,\mathrm{km\,s^{-1}\,Mpc^{-1}}$, $\Omega_\mathrm{m} = 0.27$ and $\Omega_\Lambda = 0.73$.

2 THE SAMPLE

The parent reference sample in our work is the extended 12MGS selected by Rush et al. (1993, hereafter RMS) from the *Infrared Astronomical Satellite (IRAS)* Faint Source Catalogue Version-2. The original RMS sample consists of 893 galaxies with *IRAS* 12-μm flux >0.22 Jy, 118 of which were preliminary classified as AGN (51 Seyfert 1s or quasars, 63 Seyfert 2s and 2 blazars) from existing catalogues of active galaxies (Spinoglio & Malkan 1989; Hewitt & Burbidge 1991; Veron-Cetty & Veron 1991). Although the selection of active galaxies based on their rest-frame mid-infrared (mid-IR) flux is commonly considered one of the best tools to provide almost unbiased AGN samples (e.g. Spinoglio & Malkan 1989 argue that since all galaxies emit a similar fraction of their bolometric luminosity at 12 μm, the AGN selection based on their rest-frame 12-μm flux is almost unbiased), a small anisotropy has been noted by some authors through the comparison with radio (e.g. Buchanan et al. 2006; Hönig et al. 2011) or X-ray (e.g. Gandhi et al. 2009; Asmus et al. 2014) selected samples. With this cautiousness in mind, we can none the less consider the 118 mid-IR selected, optically classified AGN to constitute one of the largest IR selected almost unbiased/mildly biased samples of AGN, likely to be almost representative of the true number and fractions of different active galaxy types in relation to each other, and thus well suited for population statistics. In support to our assumption, we note that, some authors (e.g. Gandhi et al. 2009 and Asmus et al. 2014 among many others) define the 12-μm flux as a good indicator of the intrinsic AGN continuum emission.

The 12MGS sample of AGN benefits from an extensive ancillary data set, including photometry and spectroscopy from the X-rays to radio frequencies, coming from different observational campaigns spread over the past 20 yr. In the next sub-sections we will present the multiwavelength data available for the 12MGS Seyfert sample, focusing on those used in our analysis.

2.1 Spectroscopic data

As mentioned above, the original AGN classification was based on optical data. Redshifts and optical spectroscopic data from the literature can be found in the IPAC-NED public Database. Using data from the literature, Brightman & Nandra (2011b) re-classified the 116 (excluding the two blazars) 12MGS AGN into Seyfert 1s, intermediate Seyfert 1.2–1.9s, Seyfert 2s and H II/LINERs, based on optical line ratio diagnostics, X-ray, 12 μm and [O III] luminosities and X-ray spectral properties.

Tommasin et al. (2008, 2010) presented *Spitzer*-IRS high-resolution spectra between 10 and 37 μm for 91 of the 118 AGN of the 12MGS (some of which changed their classification based on these spectroscopic data; see Tommasin et al. 2010 for details), while Wu et al. (2009) obtained low-resolution IRS spectra in the 5.5–35 μm range for 103 Seyferts of the 12MGS.

To obtain a homogeneous IRS spectroscopy data set, we re-reduced the IRS data. First, we searched for low-resolution IRS spectroscopy of 12MGS objects in the Spitzer data archive. We found 81 and 49 mapping and staring IRS observations, respectively. To reduce the data, we used the standard pipeline (version C18.18). In addition to the standard reduction, we subtracted the background emission and removed rogue pixels using IRSCLEAN with the appropriate rogue mask for each observation. For the staring observations, the spectra were extracted assuming point-like emission. For the mapping observations, we created a data cube by projecting the single pointings into a grid in a manner similar to CUBISM (Smith et al. 2007a). The spectra were extracted from the data cubes using 7.7 arcsec × 7.7 arcsec and 17.8 arcsec × 17.8 arcsec square apertures in the short-low (SL; 5.2-14 μm) and long-low (LL; 14-36 μm) cubes, respectively, centred on the nuclei. We applied an aperture correction based on the IRS mapping observations of the stars HR7341 (AOR 16295168) and HR6606 (AOR 16463104). We did this to obtain comparable spectra from both the mapping and the staring data.

In some cases, we found a mismatch in the continuum level between the SL (slit width of 3.6 arcsec) and the LL (slit width of 10.5 arcsec) spectral ranges. This can be produced by two reasons: the LL slit (or aperture) includes noticeable extended emission; or the slits were not well centred on the nucleus. Since we are interested on the IRS spectra to constrain the AGN torus, we excluded from our analysis all the spectra with a mismatch larger than 20 per cent in the continuum level at 14 μm, which may indicate that there is extended emission in the LL spectra. In total, we obtained the IRS spectra of 76 point-like sources, 56 of them with mapping observations and the rest with staring observations.

For 26 Seyfert galaxies (out of the selected 76) also the far-IR fine-structure lines have been observed with the *Herschel*-PACS and -SPIRE spectrometers, and presented by Spinoglio et al. (2015), Pereira-Santaella et al. (2013) and Fernández-Ontiveros et al. (in preparation).

Our final sample used for this study consists of 76 AGN: 42 Seyfert 1 (including 4 quasars), 27 Seyfert 2 and seven non-Seyfert galaxies (6 H II and 1 LINER). In Tables 1 and 2, we present the fluxes of the mid-IR (from Tommasin et al. 2008, 2010) and far-IR lines (from Spinoglio et al. 2015; Pereira-Santaella et al. 2013; Fernández-Ontiveros et al. in preparation) considered in this work.

2.2 X-ray data

Rush et al. (1996) studied the soft X-ray spectra of the 12MGS from *ROSAT* All-Sky Survey observations, while Barcons et al. (1995) used hard X-ray data from *HEAO 1*. Brightman & Nandra (2011a) analysed the *XMM–Newton* spectra (2–10 keV) of 126 galaxies of this sample, estimating their intrinsic power, continuum shape and obscuration levels. In a subsequent paper, Brightman & Nandra (2011b) redetermined the activity class of the 12MGS sources by way of optical line ratio diagnostics and characterized the optical class by their X-ray, 12-μm and [O III] luminosities and X-ray spectral properties. The X-ray classification has been taken into account, together with the classification based on optical and mid-IR spectra, to constrain the torus model when fitting the SED, as described in Section 3.

The 12MGS sources of our subsample have been observed in X-rays with different instruments, in different bands, during different campaigns. For the purpose of our work, we have considered the *XMM* data in the 2–10 keV range as taken from the IPAC-NED[1] public Database, which provides also the X-ray luminosity.

2.3 Photometric catalogue

To construct the broad-band SEDs of our subsample of the 12MGS, we have searched in the literature (in the IPAC-NED, Simbad[2] and Vizier[3] public Databases) for all the available data, from UV to mm. The public data were mostly patchy and derived from different observational campaigns with different instruments and photometries. When more than one observation was available for the same object in the same band, we have chosen the more recent and/or the one giving the 'total flux' (e.g. corrected for aperture).

In order to maximize the data coverage in the mid-IR range, crucial for constraining and disentangling the AGN component, we have re-binned the IRS spectral data in 2-μm intervals and added those data to the photometric SED data. Thanks to the IRS data, we were able to characterize the dusty torus model and constrain its parameters, e.g. by considering high optical depths for sources showing a strong 9.7-μm absorption feature in their spectra (see next section for details).

In Tables A1 and A2 of Appendix A, we present the photometric data for the 76 12MGS galaxies considered in this work. We stress that the sample is not a complete sample for statistical purpose. However, since it was randomly selected from a nearly complete sample, it maintains a robust statistical significance. Therefore, it can be considered as a representative sample of local the Seyfert galaxy population, for which data are available in virtually all wavebands, from UV to mm, to define their SED, including *Spitzer*-IRS spectrum (in the mid-IR range) to constrain the torus component.

Fig. 1 shows the distributions of the 12-μm flux, redshift and 12-μm luminosity for our 76 Seyfert galaxies, compared to those of the entire 12MGS optically classified AGN sample. We confirm that the objects in our study are representative of the range of properties of the 12MGS AGN: in fact, a two-sided Kolmogorov–Smirnov (K–S) test gives $P = 0.93$ ($D = 0.079$), $P = 0.67$ ($D = 0.10$) and

[1] http://ned.ipac.caltech.edu
[2] http://simbad.u-strasbg.fr/simbad/ (Wenger et al. 2000)
[3] http://vizier.u-strasbg.fr (Ochsenbein, Bauer & Marcout 2000)

Table 1. 12MGS mid-IR lines.

Name	z	[S IV]10.8	[Ne II]12.8	[Ne V]14.3	[Ne III]15.5	[S III]18.7	[Ne V]24.3	[O IV]25.9	[S III]33.5	[Si II]34.5	PAH11.2	PAH6.2
						($\times 10^{-14}$ erg s^{-1} cm^{-2})						
3C 120	0.033	24.1	7.84	16.6	27.6	7.34	29.0	123.0	17.3	36.3	···	<13.5
3C 234	0.1849	2.86	<1.29	2.35	3.4	···	2.91	8.97	···	···	···	<8.2
3C 273	0.1583	3.04	1.55	3.38	6.0	1.53	2.94	8.47	···	···	···	<21.7
3C 445	0.0562	2.75	2.31	1.95	6.23	···	5.84	22.6	<3.16	<3.69	···	···
CGCG 381−051	0.0307	<0.61	19.1	<0.7	1.35	···	<1.18	<1.26	9.36	12.5	43.8	50.7
ESO 012−G021	0.03	2.5	11.95	3.19	6.42	5.63	4.61	15.98	11.17	26.8	88.9	109.0
ESO 033−G002	0.0181	5.54	2.13	6.34	9.22	3.99	5.27	14.39	2.79	4.53	10.8	<62.5
ESO 141−G055	0.0371	3.45	2.24	2.25	5.62	1.75	1.62	7.26	5.45	8.85	19.2	···
ESO 362−G018	0.0124	1.7	12.4	3.27	7.49	3.87	2.62	8.93	7.5	11.8	71.7	66.5
IC 4329A	0.0161	29.1	27.6	29.3	57.0	15.0	34.6	117.0	16.0	32.5	···	<62.0
IC 5063	0.0113	47.4	26.7	30.3	66.3	21.8	23.6	114.0	31.0	52.7	···	21.4
IRASF 01475−074	0.0177	2.14	13.7	6.38	9.95	<4.55	1.87	6.49	3.12	<6.13	30.3	<47.4
IRASF 03450+005	0.031	1.96	1.09	<1.48	1.82	···	<1.88	2.52	1.54	<4.5	···	<65.8
IRASF 04385−082	0.0151	2.38	13.9	2.28	7.06	3.58	<1.44	8.56	<5.23	<5.36	50.5	<80.3
IRASF 05189−252	0.0426	5.63	21.12	17.53	17.76	3.18	11.73	23.71	<24.0	11.85	···	65.4
IRASF 07599+650	0.1483	<0.66	3.92	<0.75	2.45	<1.9	<3.0	<1.8	···	···	···	33.6
IRASF 08572+391	0.0583	<0.5	7.18	<0.75	1.99	1.69	<5.4	<6.0	<12.0	<25.0	···	<52.5
IRASF 13349+243	0.1076	9.3	4.8	<0.87	4.21	···	<1.47	7.35	···	···	···	<20.6
IRASF 15480−034	0.0303	5.19	5.57	6.08	9.35	2.72	8.9	35.0	5.2	5.13	49.2	<52.9
Izw 001	0.0611	6.95	2.4	4.56	6.26	···	<1.35	8.92	5.28	···	10.8	<29.0
MCG−02−33−034	0.0146	9.87	7.37	6.75	15.93	7.61	20.0	81.93	20.42	29.46	20.7	<51.1
MCG−03−34−064	0.0165	52.8	56.2	62.9	119.0	27.0	38.1	115.0	17.2	24.8	71.2	42.7
MCG−03−58−007	0.0315	2.75	8.52	6.63	9.29	5.2	3.91	8.8	<2.84	11.7	47.1	55.8
MCG−06−30−015	0.0077	8.42	4.98	5.01	5.88	6.48	7.37	26.0	6.51	9.26	25.5	<63.3
MCG+00−29−023	0.0249	<0.72	47.1	1.01	4.43	7.89	<5.42	<6.01	49.3	136.0	259.0	210.0
Mrk 0006	0.0188	16.69	28.0	9.39	49.34	14.1	10.43	48.24	14.09	36.4	20.0	<63.2
Mrk 0009	0.0399	2.37	3.23	2.21	1.9	2.38	2.24	5.55	3.94	7.32	15.2	<81.2
Mrk 0079	0.0222	10.2	10.2	6.55	19.6	8.98	12.7	42.0	14.0	30.5	13.4	<40.5
Mrk 0231	0.0422	<2.1	19.67	<3.0	3.05	<4.0	<18.0	<9.5	<8.0	16.0	···	75.0
Mrk 0273	0.0378	9.58	41.9	11.68	33.57	13.35	15.38	56.36	42.56	14.7	···	130.0
Mrk 0335	0.0258	0.43	0.25	0.38	0.61	···	1.97	7.24	<1.21	<1.45	···	<51.7
Mrk 0463	0.0504	29.86	9.25	18.25	40.78	15.85	19.93	69.17	15.5	29.79	···	<17.9
Mrk 0509	0.0344	4.13	14.0	4.74	14.5	7.19	6.82	27.5	7.41	14.5	53.9	49.2
Mrk 0704	0.0292	5.09	<3.3	3.93	5.63	<4.8	<3.75	11.8	4.3	···	···	<73.8
Mrk 0897	0.0263	<1.5	24.03	1.06	4.38	14.91	<0.8	0.62	22.3	21.44	117.0	<77.7
Mrk 1239	0.0199	6.08	9.4	3.4	9.38	1.77	3.22	15.6	9.09	10.5	34.2	<71.8
NGC 0034	0.0196	<1.46	52.1	<2.19	6.37	7.56	<0.37	<0.66	<10.7	40.5	292.0	335.0
NGC 0262	0.015	7.16	16.4	5.82	20.4	7.0	4.95	17.6	12.2	9.81	···	<57.8
NGC 0424	0.0118	8.98	8.7	16.1	18.45	6.96	6.37	25.8	9.82	8.14	19.2	<69.5
NGC 0513	0.0195	2.77	12.8	1.91	4.43	6.76	1.09	6.54	14.5	27.49	74.7	95.0
NGC 0526A	0.0191	5.32	5.77	6.35	10.4	<2.5	5.92	19.3	5.91	8.58	···	<16.0
NGC 0931	0.0167	10.7	5.47	14.3	15.41	4.86	13.67	42.6	11.97	13.72	39.5	<74.7
NGC 1056	0.0052	<1.31	33.6	<1.8	10.4	18.3	<1.23	1.4	36.6	49.1	214.0	269.0
NGC 1125	0.0109	6.07	16.37	5.09	15.55	10.99	9.69	40.36	23.94	31.32	64.2	77.5
NGC 1194	0.0136	5.05	3.81	4.28	7.37	<2.25	3.76	15.1	3.98	3.6	···	<50.5
NGC 1320	0.0089	9.01	9.58	10.7	13.6	4.15	7.46	27.4	12.0	10.4	51.5	68.6
NGC 1365	0.0055	18.6	143.0	19.1	61.3	51.2	97.5	365.0	720.0	1303.0	57.0	1730.0
NGC 1566	0.0050	<2.04	17.22	0.97	9.42	6.98	···	6.12	7.37	15.0	···	276.0
NGC 2992	0.0077	26.6	53.5	23.3	49.4	28.6	23.2	103.0	74.7	109.0	115.0	153.0
NGC 3079	0.0037	<1.21	181.0	<2.57	24.5	12.7	<2.66	12.7	42.1	166.0	540.0	1110.0
NGC 3516	0.0088	13.33	8.07	7.88	17.72	5.86	10.39	46.92	9.52	22.14	25.8	<65.7
NGC 4051	0.0023	4.75	21.2	10.7	17.1	7.45	32.2	94.6	38.8	39.6	133.0	92.0
NGC 4151	0.0033	89.6	122.0	71.7	205.0	71.4	81.7	261.0	77.6	147.0	···	<69.8
NGC 4253	0.0129	12.2	23.3	21.0	24.1	12.8	18.5	46.1	21.4	15.5	58.5	30.8
NGC 4388	0.0084	45.3	76.6	46.1	106.0	39.1	73.0	340.0	85.1	135.0	103.0	150.0
NGC 4593	0.0090	5.5	7.34	3.09	8.13	3.94	<4.32	33.3	19.1	32.2	44.5	48.2
NGC 4602	0.0085	<1.2	7.57	0.82	0.63	3.2	<1.2	<2.3	8.68	15.3	28.2	46.1
NGC 5135	0.0137	6.07	36.7	4.88	16.7	11.4	15.2	71.3	38.3	140.0	124.0	416.0
NGC 5256	0.0279	2.57	19.8	2.31	10.6	8.38	11.9	56.8	48.2	92.3	41.0	199.0
NGC 5347	0.0078	<2.41	4.17	2.08	4.09	<2.86	<1.74	7.64	<3.38	<4.6	33.2	<43.7
NGC 5506	0.0062	25.4	26.4	18.5	45.6	19.1	56.5	239.0	90.1	137.0	34.8	108.0
NGC 5548	0.0172	6.37	8.47	5.4	7.27	5.93	3.89	17.5	<4.14	12.46	34.9	10.8
NGC 5953	0.0066	1.52	67.2	2.24	16.7	22.3	6.44	21.0	80.1	145.0	239.0	529.0

Table 1 – *continued*

Name	z	[S IV]10.8	[Ne II]12.8	[Ne V]14.3	[Ne III]15.5	[S III]18.7	[Ne V]24.3	[O IV]25.9	[S III]33.5	[Si II]34.5	PAH11.2	PAH6.2
						($\times 10^{-14}$ erg s^{-1} cm^{-2})						
NGC 5995	0.0252	5.71	16.5	6.13	8.47	4.22	3.11	12.9	5.32	25.4	91.2	82.5
NGC 6810	0.0068	<1.09	103.0	<1.09	13.4	41.0	<2.35	2.55	78.2	118.0	91.2	561.0
NGC 6860	0.0149	3.36	5.6	2.85	6.65	2.8	2.41	12.1	7.93	10.4	21.7	63.2
NGC 6890	0.0081	2.92	11.32	5.77	6.57	4.34	3.77	10.1	16.97	26.54	48.8	96.6
NGC 7130	0.0162	5.27	79.3	9.09	29.4	19.6	5.22	19.7	48.2	93.9	216.0	327.0
NGC 7213	0.0058	2.32	25.7	<1.85	12.0	5.0	<0.89	<13.5	6.97	15.7	62.2	17.3
NGC 7469	0.0163	10.5	179.0	17.5	37.5	75.1	17.1	22.9	76.8	198.0	482.0	608.0
NGC 7496	0.0055	1.3	48.08	<1.8	6.67	23.48	<2.4	<2.4	39.47	44.58	153.0	446.0
NGC 7603	0.0295	<0.72	12.5	<0.75	5.71	4.94	<0.93	3.52	9.27	18.7	65.3	70.8
NGC 7674	0.0289	16.1	20.1	21.2	35.3	...	16.5	49.3	14.4	29.7	84.6	142.0
TOLOLO 1238−364	0.0109	5.7	45.15	11.15	27.0	16.32	5.35	21.21	32.8	44.99	111.0	151.0
UGC 05101	0.0394	0.91	34.13	2.57	13.66	5.57	2.82	7.35	15.46	32.07	...	123.0
UGC 07064	0.025	4.03	8.15	4.16	6.65	4.04	5.17	14.0	9.22	10.7	42.1	79.0

Table 2. 12MGS far-IR lines.

Name	[O III]52	[N III]57	[O I]63	[O III]88	[N II]122	[O I]145	[C II]158
				($\times 10^{-14}$ erg s^{-1} cm^{-2})			
3C 120	58.38	...	20.42	73.48	...	59.75	44.47
3C 234	...	...	1.49	...	...	...	...
IRASF 03450+0055	...	...	...	...	...	...	2.12
IRASF 05189−2524	...	62.19	14.12	...	3.08	2.60	17.85
IRASF 13349+2438	...	...	8.46	...	...	...	...
MCG−03−34−064	...	...	70.28	28.45	...	...	26.59
MCG−06−30−015	...	...	...	...	...	...	5.95
Mrk 0009	...	...	...	...	...	...	12.97
Mrk 0231	...	2.06	29.67	14.73	3.32	3.53	44.82
Mrk 0273	...	11.46	39.62	40.33	18.54	8.06	90.75
Mrk 0509	...	...	25.64	16.69	...	0.92	36.15
NGC 1365	...	136.83	431.82	198.16	255.96	22.01	1102.92
NGC 3079	...	...	...	...	...	...	726.42
NGC 3516	...	...	19.22	28.68	6.80	...	21.61
NGC 4051	...	...	30.92	6.86	3.85	2.80	42.91
NGC 4151	16.31	22.60	322.48	44.68	7.34	19.04	64.57
NGC 4388	...	19.37	221.37	137.44	10.78	15.24	238.46
NGC 4593	...	...	...	...	3.03	2.94	20.53
NGC 5135	...	...	140.87	65.54	...	10.17	228.33
NGC 5347	...	...	...	...	...	...	12.78
NGC 5506	30.16	34.92	163.30	106.16	15.00	14.29	121.69
NGC 5548	...	...	...	...	...	...	17.63
NGC 6860	...	...	...	...	...	...	41.92
NGC 7213	...	...	...	...	...	...	31.98
NGC 7469	...	50.61	232.03	26.43	42.12	18.15	290.12
NGC 7603	...	...	...	...	...	...	37.58
NGC 7674	...	...	57.82	25.15	...	...	111.38

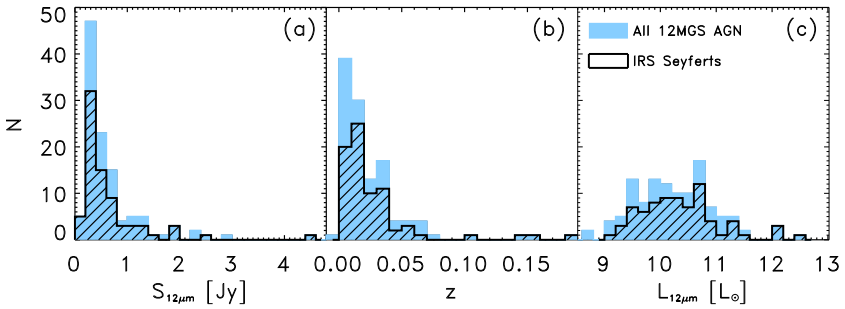

Figure 1. Distribution of (a) 12-μm flux, (b) redshift and (c) 12-μm luminosity of the 76 Seyferts with *Spitzer*-IRS low-resolution spectra (black hatched histogram) versus entire 12MGS sample of optically classified AGN (blue filled histogram).

$P = 0.87$ ($D = 0.082$) for the 12-μm flux, the redshift and the 12-μm luminosity, respectively.

3 BROAD-BAND SED DECOMPOSITION

The rest-frame SEDs of the galaxies in the sample have been fitted with a three components model using the approach described by Berta et al. (2013). The adopted code was inspired by MAGPHYS (da Cunha, Charlot & Elbaz 2008) for the stellar and dusty SF part, but it effectively combines three components simultaneously, i.e. including AGN/torus emission. Due to the huge number of possible combinations, the code samples the parameters space randomly, allowing for roughly 10^9 possible combinations at each iteration. We defer to Berta et al. (2013) for further details about the code.

The adopted libraries are the Bruzual & Charlot (2003) stellar library (see also da Cunha et al. 2008), the da Cunha et al. (2008) IR dust-emission library and the library of AGN tori by Fritz, Franceschini & Hatziminaoglou (2006), updated by Feltre et al. (2012). The latter includes both the emission of the dusty torus, heated by the central AGN engine, and the emission of the accretion disc. Note that the considered AGN models are based on a continuous (e.g. 'smooth') distribution of dust across the torus; we have not tested the technique with clumpy torus models. For a direct comparison smooth versus clumpy torus see Feltre et al. (2012).

The AGN library comprises a total of 2376 models, each 'observed' from 10 different viewing angles spanning the 0–90 deg range with respect to the torus equatorial plane. The geometry of the torus varies as parametrized by its opening angle of the torus, Θ, and the ratio between the outer and inner radius of the dust distribution, $R_{\rm m}$. The dust density distribution is parametrized as $\rho(r, \theta) = Ar^{\beta}\exp(-\gamma\cos(\theta))$, as a function of the vertical (θ) and radial (r) coordinates, with exponents γ and β. If (γ, β) = (0,0), there is no variation of the dust density in either the vertical or radial direction. Finally $\tau_{9.7}$ is the reference optical depth of the torus on the equatorial plane, computed at 9.7 μm and integrated over the whole extent of the torus.

Due to degeneracies between the parameters (see Hatziminaoglou, Fritz & Jarrett 2009; Pozzi et al. 2010), we limit the analysis to $\gamma = 0.0$ and $\beta = -1.0, -0.5, 0.0$. Moreover, we constrain $R_{\rm m} \leq 100$ (Netzer et al. 2007; Mullaney et al. 2011), in order to avoid too large and cold tori.

The wealth of information available for the 12MGS sample can be used to further constrain the torus library and properties, so to reduce degeneracies. More specifically, the X-ray spectra allow an estimate of the column density $N_{\rm H}$. In parallel, the presence or absence of the 9.7 μm silicate feature in absorption in the mid-IR spectra provides hints on the most reasonable $\tau_{9.7}$ range to be used. Finally, optical and X-ray classifications, as well as optical/mid-IR SED shapes can put constraints on the most convenient viewing angles to be used. Hence we combine these three pieces of information to further reduce the number of models, and include/avoid those with strong absorption or improper viewing angles in the fit, for each specific case. In particular, we use the information about $N_{\rm H}$ from X-rays and the presence/absence of the 9.7 μm feature to reduce the number of possible torus solutions for each source, e.g. by excluding all the torus models with no 9.7 μm feature in absorption for objects with high $N_{\rm H}$ and/or with that feature observed in the IRS spectrum. Vice versa, we have excluded the 'obscured'/'optically thick' models for objects with low column density and/or no 9.7 μm feature in absorption in the IRS spectrum. Analogously, we have used the information from optical spectroscopy (e.g. Seyfert 1 or 2 based on broad or narrow lines and BPT diagrams; Baldwin, Phillips & Terlevich 1981): in case of objects spectroscopically classified as type 1/'broad-line', we have considered only 'unobscured' torus models, with the optical/UV spectrum provided by the AGN/disc and not by the stellar component. Vice versa, for objects classified as type 2, we have considered only models with depressed/absorbed optical/UV light, letting it to be reproduced by the host galaxy stellar contribution.

In this way, the random sampling of the torus library avoids to waste computing time on models that will be in any case discarded, and focuses on a finer sampling of the appropriate torus parameters range.

Note that the chosen torus library can in principle be changed and selected among all the sets available in the literature, either 'smooth' (e.g. Pier & Krolik 1992; Granato & Danese 1994; Fritz et al. 2006), 'clumpy' (e.g. Nenkova et al. 2008; Hönig & Kishimoto 2010) or 'composite' (e.g. Stalevski et al. 2012).

In Fig. 2, we show few examples of observed 12MGS SEDs decomposed into stellar, AGN and SF components using the above described technique. The torus emission, when needed by the fit, is shown as green dashed line. The decomposition code provides a probability distribution function (PDF) in each photometric band and for each fit component, allowing an estimate of the uncertainty related to each decomposed contribution. In Fig. 3, we show an example of an observed SED, with the galaxy and AGN components defined by their uncertainty regions obtained through the PDF analysis (green for the torus and red for the host galaxy). The IRS spectrum associated with the same 12MGS object is also shown (and zoomed) in a separate panel.

4 RESULTS

In Table 3, we report the main results obtained from the SED-fitting decomposition described in the previous section. In particular, in columns 2, 3, 4, 5, 6 and 7, for each source we list the total IR luminosity (obtained by integrating the SED in the 8–1000 μm rest-frame, $L_{\rm IR}^{\rm TOT}$), the SFR (obtained through the Kennicutt 1998 relation converted to a Chabrier IMF), the IR luminosity due to SF ($L_{\rm IR}^{\rm SF}$), the IR luminosity due to AGN accretion($L_{\rm IR}^{\rm AGN}$), the fraction of 5–40 μm luminosity produced by an AGN ($f_{\rm AGN}$(5–40)) and the AGN bolometric luminosity ($L_{\rm bol}^{\rm AGN}$), respectively. The AGN bolometric luminosity is obtained through a bolometric correction (BC) available for each AGN template. The BC allows us to calculate $L_{\rm bol}^{\rm AGN}$ directly from the IR (1–1000 μm rest frame) luminosity of the best-fitting AGN model. In the last three columns, for comparison, we report the AGN bolometric luminosity derived from the X-ray (by Brightman & Nandra 2011a), the [Ne V]14.3 and 24.3 μm and the [O IV]25.9 μm luminosities (by Tommasin et al. 2010), respectively. The uncertainties associated with the parameters derived through the SED decomposition have been obtained from the PDF distribution provided by the fitting routine.

The SED decomposition code provides the fraction of luminosity due to the AGN in several IR bands (1–5, 5–10, 10–20, 5–40 and 8–1000 μm): for our purpose we have chosen to represent the different AGN fractions in the 5–40 μm band, since it is large enough not to be too sensitive to small-scale variations like PAHs, but it is where the AGN contribution – if any – should come out and be maximized with respect to stellar and SF ones.

4.1 AGN fraction

In Fig. 4, we show the fraction of luminosity due to the AGN in the 5–40 μm range versus redshift for type 1 and type 2 AGN. On the

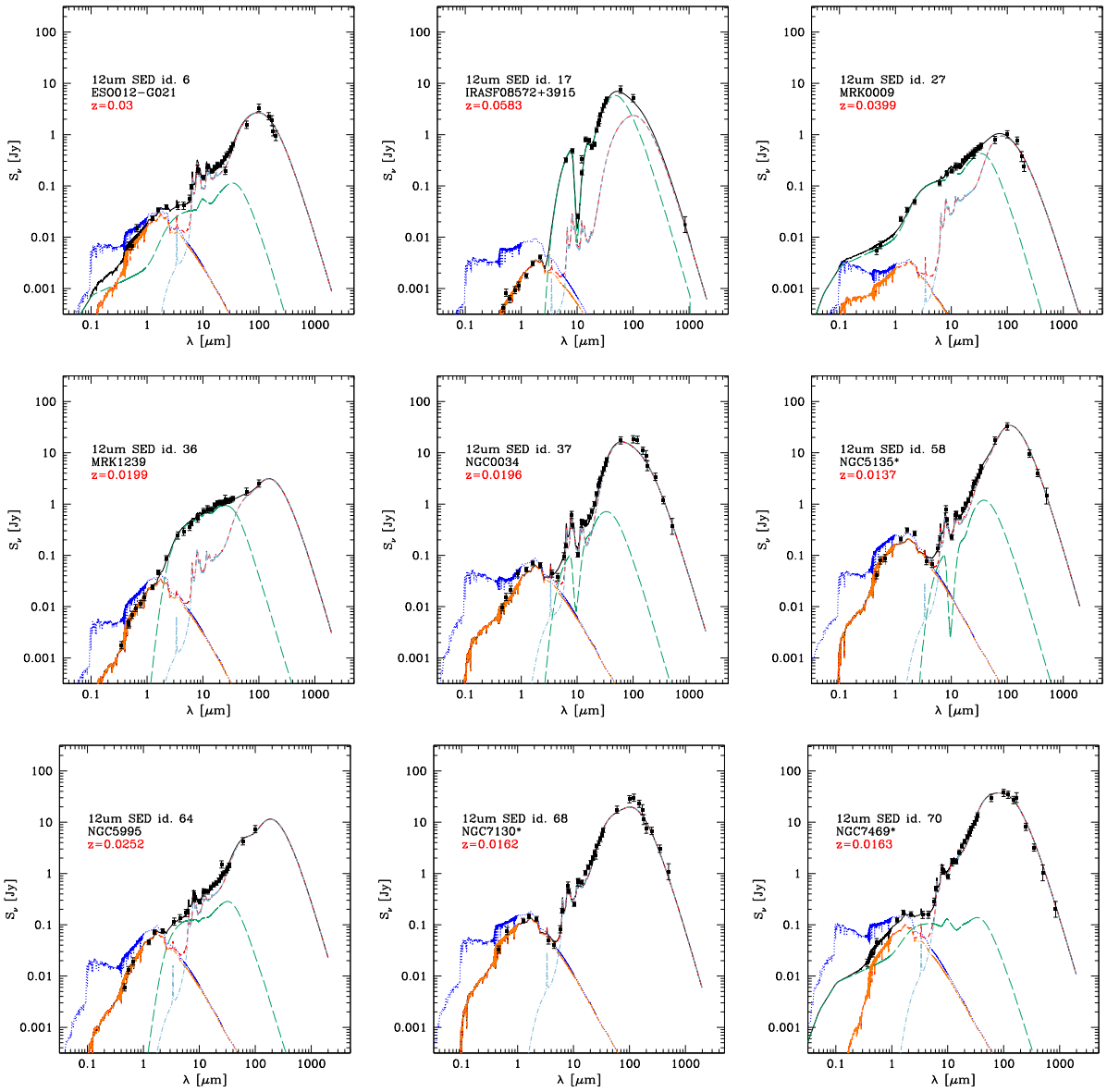

Figure 2. Example of observed SEDs decomposed into stellar, AGN and SF components using the technique developed by Berta et al. (2013). The black filled circles with error bars are our data (with IRS spectra rebinned, as described in the text). Blue dotted lines show the unabsorbed stellar component, red dashed lines show the combination of extinguished stars and dust IR emission, while long-dashed green lines show the dusty torus emission. Pale-blue dot–dashed lines show the dust re-emission, while black solid lines are the sum of all components (total emission).

top and along the right axis, we plot also the redshift distribution and the 5–40 μm AGN fraction distribution. While there is basically no difference in the z-distribution for AGN 1 and 2 (apart from 4 type 1 sources at $0.1 < z < 0.2$ and no type 2's in that range), type 2 AGN tend to have lower AGN fractions than type 1s (more numerous at higher AGN fractions), although the total (type1+type2) AGN fraction distribution is almost flat. We note that the optical classification is biased against obscuration/torus orientation and often does not match with X-ray type 1/type 2 definition or with IR/SED-fitting classification. However, the general trend of type 1 AGN showing higher intrinsic AGN fractions is not surprising, since it has been shown statistically in table 8 of Tommasin et al. (2010) for this specific sample, and it is also in agreement with the results of other works (i.e. Veilleux et al. 2009; Brightman & Nandra 2011a; Netzer 2015 and references therein).

In Fig. 5, we show the fraction of luminosity due to the AGN in the 5–40 μm range against that in the 8–1000 μm range, and the ratio between the two fractions versus the [O IV] 25.9 μm luminosity, for the different types of 12MGS galaxies – i.e. Seyfert 1/1.5/1.8/1.9/2 and non-Seyfert, as defined through optical spectroscopy and 12 μm and X-ray luminosity. From the former diagram it is clear that, even if this sample is biased towards AGN-dominated objects (showing significantly high fractions of the total IR luminosity due to AGN), in the 5–40 μm band, the AGN contribution is always higher than in the 8–1000 μm range. The two contributions become similar for objects showing the highest AGN fractions (e.g. totally dominated by the AGN). We can also notice that Seyfert 1/1.5 galaxies show, on average, higher $L_{[\mathrm{O\,IV}]}$ and higher AGN fractions (both at 5–40 and 8–1000 μm), but tend to populate the lower $f_{\mathrm{AGN}}(5\text{–}40)/f_{\mathrm{AGN}}(8\text{–}1000)$ part of the diagram

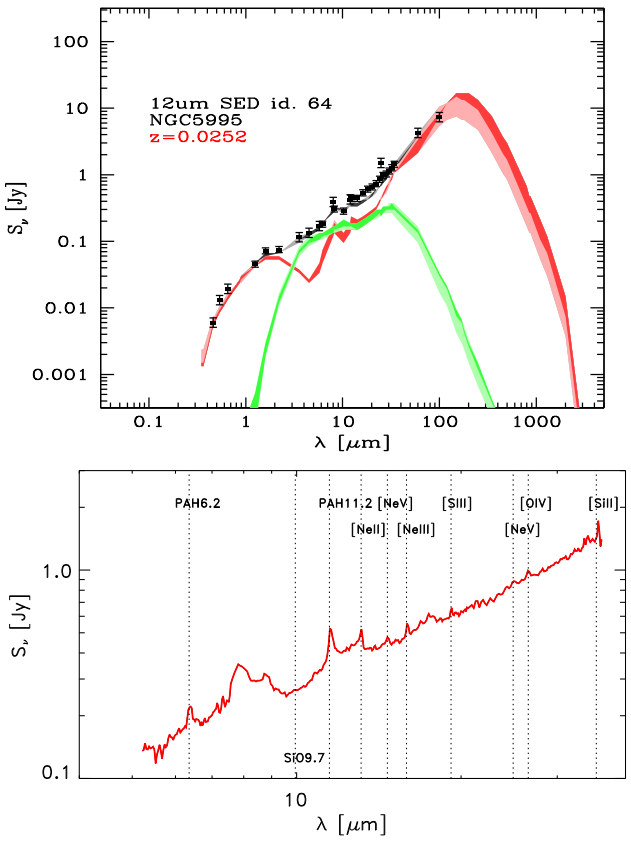

Figure 3. Example of decomposed SED, with PDF uncertainty regions associated with the AGN (green) and galaxy (red) components highlighted as coloured bands (top panel). Bottom panel: IRS spectrum associated with the 12MGS source.

(e.g. have higher far-IR to mid-IR luminosity ratios). The AGN-dominated objects (those with $f_{\rm AGN}(5–40)/f_{\rm AGN}(8–1000) \sim 1$ and both, $L(8–1000\,\mu{\rm m})$ and $L(5–40\,\mu{\rm m})$ dominated by the AGN) are more likely to be optically classified as type 1 than type 2. On the contrary, the non-Seyfert/LINER classified objects are mostly at higher $f_{\rm AGN}(5–40)/f_{\rm AGN}(8–1000)$ (e.g. dominate the mid-IR rather than the far-IR) and (as expected) have lower [O IV] luminosities. Seyfert 2/1.9/1.8 galaxies are spread over the whole range of AGN fraction ratios and luminosities. Low [O IV] luminosities seem to correspond to higher mid-to-far-IR fraction ratios. This can be interpreted as the far-IR range to be dominated by SF, as expected for low-luminosity AGN as LINERs, with the AGN showing up mostly in the mid-IR, where the galaxy SED shows a dip.

We have applied a two sample K–S test, to provide an assessment of the likelihood that the Seyfert 1s and Seyfert 2s samples were drawn from the same parent distribution. First, we have considered the Seyfert 1's and Seyfert 2's distributions plotted in Fig. 5, including the intermediate types (1.5/1.8/1.9) in the Seyfert 2 category. We derive that the probability that the two distributions are drawn from the same parent one is $P = 0.03$ (the test statistic, or the maximum difference, is $D = 0.299$). Then we have performed again the test, by considering all the intermediate types in the Seyfert 1 class. As a result, this time we found $P = 0.06$ ($D = 0.359$). Therefore, in both cases, the two cumulative frequency distributions are more likely to be randomly sampled from populations with different distributions, although the significance of this difference is only about 2σ.

4.2 AGN bolometric luminosity

In Fig. 6, the AGN bolometric luminosity that we derive from the SED decomposition (e.g. from the best-fitting torus model) is compared to the same quantity obtained by means of different methods: i.e. from the 2–10 keV X-ray luminosity (from IPAC-NED public Database), and the AGN mid-IR line luminosity (e.g. [Ne V] and [O IV]; Tommasin et al. 2008, 2010). The agreement is good, especially with the mid-IR line derivations (scatter around the 1–1 relations: $\sigma_X = 1.11, \sigma_{[\rm Ne\,V]14.3} = 0.61, \sigma_{[\rm Ne\,V]24.3} = 0.66, \sigma_{[\rm O\,IV]25.9} = 0.7$). The significance level associated with these correlations has been derived by calculating the Spearmans partial rank correlation coefficients between two variables independent on a third (the distance in our case), by following the method described by Macklin (1982). The resulting significance level of these relations is $1.5\sigma, 3.4\sigma, 3.3\sigma$ and 3.2σ for the AGN luminosity derived from X-ray, [Ne V]14.3, [Ne V]24.3 and [O IV]25.9, respectively.

We note that the relation between SED fitting and X-ray derived AGN bolometric luminosity is more dispersed and with a lower significance than those with mid-IR AGN lines. This is likely due to a significant number of objects showing values of the AGN bolometric luminosity estimated from the X-ray band lower than those derived by decomposing the SED. These objects are well-known obscured AGN (with weak X-ray emission, i.e. IRASF 07599+6508, IRASF 08572+3915, Mrk 0231, UGC05101), for which the intrinsic X-ray luminosity obtained by means of a correction for obscuration may be underestimated. Moreover, most of the objects deviating from the relations are at relatively low X-ray luminosities ($<10^{43.5}$ erg s^{-1}), where the X-ray classification as AGN is less certain and the contamination due to starburst can be significant (e.g. Brightman & Nandra 2011b consider'unambiguos X-ray AGN' only sources with an observed 2–10 keV luminosity greater than 10^{42} erg s^{-1}).

We are testing these hypothesis by re-analysing the X-ray spectra of the 12MGS, including also recent data from the *Nuclear Spectroscopic Telescope Array* (*NuSTAR*; Harrison et al. 2013), when available (Vignali et al. in preparation). Indeed, the objects showing larger deviance from the relation are also known to be highly obscured AGN from the literature (e.g. some of them being Compton thick, CT: $N_{\rm H} \gtrsim 10^{24}$ cm^{-2}). Note that the objects for which we find a higher fraction of mid-IR luminosity due to the AGN are also those with higher bolometric luminosities.

4.3 The AGN-SF connection

In Fig. 7, we plot the IR luminosity due to SF ($L_{\rm IR}^{\rm SF}$) versus the AGN bolometric luminosity ($L_{\rm bol}^{\rm AGN}$), using different colours to highlight sources with different AGN fractions. A correlation between the two quantities plotted here has been found in the literature for QSOs (at $z \sim 0$: Netzer et al. 2007, and at $z = 2–3$: Lutz et al. 2008) and for type II AGN (Netzer 2009), with a slope of about 0.8 ($L^{\rm SF} \propto (L_{\rm bol}^{\rm AGN})^{0.8}$). More recent studies, based on *Herschel* data up to $z \sim 2–3$ (Shao et al. 2010; Rosario et al. 2012) demonstrate that the $L^{\rm SF}$–$L^{\rm AGN}$ plane can be divided into two regimes with very different behaviours. One is the 'SF-dominated' regime, where $L^{\rm SF} > L^{\rm AGN}$, and the two properties are not correlated and $L^{\rm SF}$ exceeds $L^{\rm AGN}$ by a factor that depends on redshift. In the second 'AGN-dominated' regime, where $L^{\rm AGN} > L^{\rm SF}$, the two luminosities seem to correlate as $L^{\rm SF} \propto (L^{\rm AGN})^{0.7}$. In all these works, the assumption is that the 60 μm luminosity is totally due to SF ($L_{\rm SF} = \nu L_\nu(60\,\mu{\rm m})$); moreover the way the samples are selected strongly affects the distribution in the $L^{\rm SF}$–$L^{\rm AGN}$ plane (e.g. Harrison et al. 2012; Page et al.

Table 3. Main properties from SED-fitting decomposition of the 76 12MGS Seyfert galaxies.

Name	$\log(L_{\rm IR})$	SFR	$\log(L_{\rm IR}^{\rm SF})$	$f_{\rm AGN}(5–40)$	$\log(L_{\rm bol}^{\rm AGN})$			
					IR	X-ray	[Ne V]	[O IV]
	$\log(L_\odot)$	$M_\odot\ yr^{-1}$	$\log(L_\odot)$		$\log(L_\odot)$			
3C 120	11.36 ± 0.01	13.83 ± 0.07	11.14 ± 0.01	0.77 ± 0.05	11.50 ± 0.14	12.33 ± 0.39	12.10 ± 0.24	12.44 ± 0.36
3C 234	12.18 ± 0.02	51.56 ± 3.45	11.71 ± 0.07	0.88 ± 0.01	13.02 ± 0.01	···	13.11 ± 0.20	13.06 ± 0.24
3C 273	12.66 ± 0.02	160.80 ± 0.75	12.21 ± 0.07	0.89 ± 0.03	13.06 ± 0.02	14.53 ± 0.72	13.13 ± 0.20	12.83 ± 0.16
3C 445	11.22 ± 0.01	4.48 ± 0.20	10.65 ± 0.04	0.96 ± 0.01	11.70 ± 0.01	12.67 ± 0.44	11.49 ± 0.03	12.08 ± 0.22
CGCG 381−051	11.12 ± 0.01	13.26 ± 0.07	11.12 ± 0.01	0.01 ± 0.42	9.48 ± 0.27	···	<10.22	<9.78
ESO 012−G021	11.02 ± 0.03	9.35 ± 1.12	10.97 ± 0.12	0.26 ± 0.07	10.46 ± 0.19	10.88 ± 0.20	11.06 ± 0.17	11.17 ± 0.20
ESO 033−G002	10.58 ± 0.01	2.86 ± 0.02	10.46 ± 0.01	0.61 ± 0.02	10.76 ± 0.01	10.80 ± 0.12	10.89 ± 0.07	10.56 ± 0.01
ESO 141−G055	11.14 ± 0.04	7.12 ± 0.74	10.85 ± 0.10	0.86 ± 0.02	11.43 ± 0.02	11.98 ± 0.30	11.12 ± 0.01	10.97 ± 0.02
ESO 362−G018	10.23 ± 0.03	1.23 ± 0.15	10.09 ± 0.12	0.48 ± 0.60	10.69 ± 0.30	10.22 ± 0.01	10.13 ± 0.10	9.90 ± 0.14
IC 4329A	10.85 ± 0.01	2.00 ± 0.08	10.30 ± 0.04	0.88 ± 0.02	11.53 ± 0.00	11.95 ± 0.27	11.66 ± 0.11	11.64 ± 0.13
IC 5063	10.84 ± 0.03	5.28 ± 0.63	10.72 ± 0.12	0.46 ± 0.05	11.27 ± 0.30	10.51 ± 0.05	11.18 ± 0.04	11.13 ± 0.04
IRASF 01475−0740	10.59 ± 0.03	3.49 ± 0.42	10.54 ± 0.12	0.25 ± 0.60	9.97 ± 0.05	10.17 ± 0.11	10.80 ± 0.20	10.04 ± 0.01
IRASF 03450+0055	10.94 ± 0.01	4.01 ± 0.11	10.60 ± 0.03	0.83 ± 0.02	11.19 ± 0.01	···	<10.67	10.19 ± 0.16
IRASF 04385−0828	10.83 ± 0.03	3.36 ± 0.28	10.53 ± 0.08	0.71 ± 0.03	11.25 ± 0.02	···	10.12 ± 0.20	10.07 ± 0.20
IRASF 05189−2524	12.21 ± 0.03	155.30 ± 18.64	12.19 ± 0.12	0.12 ± 0.04	11.80 ± 0.03	11.12 ± 0.01	12.45 ± 0.27	11.80 ± 0.12
IRASF 07599+6508	12.55 ± 0.04	283.00 ± 9.00	12.45 ± 0.03	0.43 ± 0.17	12.46 ± 0.05	9.29 ± 0.51	<12.16	<11.84
IRASF 08572+3915	12.09 ± 0.02	24.31 ± 2.79	11.39 ± 0.11	0.95 ± 0.60	12.90 ± 0.01	···	<11.04	<11.41
IRASF 13349+2438	12.21 ± 0.01	21.89 ± 1.79	11.34 ± 0.08	0.98 ± 0.01	12.76 ± 0.14	11.93 ± 0.01	<11.85	12.26 ± 0.06
IRASF 15480−0344	11.11 ± 0.12	10.16 ± 1.34	11.01 ± 0.13	0.52 ± 0.10	11.51 ± 0.30	9.46 ± 0.32	11.46 ± 0.06	11.64 ± 0.13
Izw 001	11.86 ± 0.01	41.84 ± 0.64	11.62 ± 0.02	0.73 ± 0.01	11.91 ± 0.06	11.68 ± 0.12	12.08 ± 0.15	11.65 ± 0.06
MCG−02−33−034	10.41 ± 0.02	2.55 ± 0.04	10.41 ± 0.02	0.01 ± 0.67	8.26 ± 0.88	···	10.76 ± 0.51	11.35 ± 0.65
MCG−03−34−064	11.06 ± 0.03	5.65 ± 0.56	10.75 ± 0.10	0.72 ± 0.07	11.48 ± 0.15	11.59 ± 0.18	12.14 ± 0.25	11.67 ± 0.15
MCG−03−58−007	11.37 ± 0.04	20.15 ± 0.88	11.30 ± 0.04	0.48 ± 0.07	11.60 ± 0.02	···	11.49 ± 0.05	10.85 ± 0.08
MCG−06−30−015	9.88 ± 0.03	0.49 ± 0.06	9.69 ± 0.12	0.60 ± 0.02	10.26 ± 0.01	10.59 ± 0.16	9.96 ± 0.06	10.07 ± 0.04
MCG+00−29−023	11.31 ± 0.03	18.71 ± 0.55	11.27 ± 0.03	0.34 ± 0.13	11.23 ± 0.21	···	10.29 ± 0.16	<10.48
Mrk 0006	10.93 ± 0.03	7.46 ± 0.02	10.87 ± 0.00	0.48 ± 0.03	10.45 ± 0.03	11.30 ± 0.31	11.14 ± 0.19	11.26 ± 0.23
Mrk 0009	11.11 ± 0.02	5.72 ± 0.35	10.76 ± 0.06	0.81 ± 0.04	11.28 ± 0.04	11.15 ± 0.11	11.20 ± 0.04	10.92 ± 0.01
Mrk 0079	10.85 ± 0.02	3.37 ± 0.10	10.53 ± 0.03	0.86 ± 0.04	11.59 ± 0.31	11.35 ± 0.10	11.15 ± 0.03	11.39 ± 0.05
Mrk 0231	12.51 ± 0.01	188.10 ± 5.50	12.27 ± 0.03	0.62 ± 0.09	12.74 ± 0.04	10.21 ± 0.39	<11.44	<11.29
Mrk 0273	11.92 ± 0.03	66.85 ± 8.02	11.83 ± 0.12	0.39 ± 0.02	11.86 ± 0.30	10.75 ± 0.10	12.08 ± 0.16	12.17 ± 0.21
Mrk 0335	10.71 ± 0.03	1.59 ± 0.16	10.20 ± 0.10	0.89 ± 0.02	10.96 ± 0.02	11.15 ± 0.17	9.72 ± 0.24	10.52 ± 0.05
Mrk 0463	11.67 ± 0.02	15.40 ± 2.03	11.19 ± 0.13	0.87 ± 0.02	12.50 ± 0.30	11.20 ± 0.12	12.70 ± 0.20	12.64 ± 0.22
Mrk 0509	11.10 ± 0.03	5.09 ± 0.45	10.71 ± 0.09	0.83 ± 0.02	11.50 ± 0.02	12.17 ± 0.34	11.42 ± 0.06	11.60 ± 0.12
Mrk 0704	10.85 ± 0.01	1.09 ± 0.07	10.04 ± 0.07	0.93 ± 0.01	11.28 ± 0.00	10.88 ± 0.04	11.20 ± 0.04	11.02 ± 0.02
Mrk 0897	11.46 ± 0.03	28.23 ± 3.39	11.45 ± 0.12	0.08 ± 0.02	10.81 ± 0.01	···	10.24 ± 0.10	9.23 ± 0.30
Mrk 1239	10.93 ± 0.02	3.47 ± 0.26	10.54 ± 0.08	0.87 ± 0.06	11.31 ± 0.03	10.79 ± 0.01	10.71 ± 0.08	10.76 ± 0.05
NGC 0034	11.42 ± 0.05	24.44 ± 1.79	11.39 ± 0.07	0.19 ± 0.10	11.03 ± 0.05	9.79 ± 0.17	<10.33	<8.98
NGC 0262	10.53 ± 0.04	1.35 ± 0.19	10.13 ± 0.14	0.79 ± 0.03	11.34 ± 0.02	10.66 ± 0.03	10.55 ± 0.12	10.38 ± 0.15
NGC 0424	10.56 ± 0.01	1.26 ± 0.05	10.10 ± 0.04	0.80 ± 0.03	11.19 ± 0.01	10.77 ± 0.03	10.84 ± 0.03	10.32 ± 0.13
NGC 0513	10.83 ± 0.07	6.64 ± 0.44	10.82 ± 0.07	0.08 ± 0.30	10.19 ± 0.28	···	10.26 ± 0.02	10.16 ± 0.00
NGC 0526A	10.74 ± 0.01	4.99 ± 0.03	10.70 ± 0.01	0.40 ± 0.11	10.31 ± 0.17	11.22 ± 0.32	10.90 ± 0.16	10.72 ± 0.11
NGC 0931	10.87 ± 0.02	5.90 ± 0.71	10.77 ± 0.12	0.40 ± 0.11	10.98 ± 0.09	9.90 ± 0.13	10.95 ± 0.04	10.76 ± 0.06
NGC 1056	9.82 ± 0.01	0.66 ± 0.01	9.82 ± 0.01	···	···	···	<9.29	8.46 ± 0.05
NGC 1125	10.40 ± 0.02	2.23 ± 0.06	10.35 ± 0.02	0.28 ± 0.13	10.26 ± 0.08	···	10.11 ± 0.03	10.45 ± 0.05
NGC 1194	10.21 ± 0.02	0.60 ± 0.03	9.78 ± 0.05	0.79 ± 0.04	11.16 ± 0.04	10.35 ± 0.07	10.30 ± 0.15	10.21 ± 0.15
NGC 1320	10.10 ± 0.01	0.92 ± 0.01	9.96 ± 0.01	0.56 ± 0.01	10.58 ± 0.06	···	10.37 ± 0.02	10.12 ± 0.08
NGC 1365	11.22 ± 0.03	15.74 ± 0.58	11.20 ± 0.04	0.12 ± 0.60	10.47 ± 0.52	9.46 ± 0.14	9.90 ± 0.11	10.71 ± 0.08
NGC 1566	10.64 ± 0.02	4.32 ± 0.07	10.64 ± 0.02	0.05 ± 0.33	9.23 ± 0.16	···	7.71 ± 0.32	7.90 ± 0.30
NGC 2992	10.58 ± 0.07	3.61 ± 0.26	10.56 ± 0.07	0.35 ± 0.03	10.13 ± 0.06	10.40 ± 0.14	10.57 ± 0.11	10.60 ± 0.11
NGC 3079	10.60 ± 0.01	3.81 ± 0.04	10.58 ± 0.01	0.20 ± 0.10	10.03 ± 0.25	7.65 ± 0.39	<8.97	9.06 ± 0.21
NGC 3516	10.17 ± 0.02	1.02 ± 0.05	10.01 ± 0.05	0.60 ± 0.12	10.27 ± 0.01	10.69 ± 0.19	10.25 ± 0.00	10.44 ± 0.05
NGC 4051	9.45 ± 0.03	0.25 ± 0.03	9.40 ± 0.12	0.30 ± 0.10	8.88 ± 0.30	9.02 ± 0.04	9.21 ± 0.02	9.59 ± 0.08
NGC 4151	9.80 ± 0.01	0.29 ± 0.01	9.46 ± 0.03	0.77 ± 0.03	10.56 ± 0.02	10.38 ± 0.05	10.58 ± 0.03	10.51 ± 0.02
NGC 4253	10.64 ± 0.03	3.99 ± 0.17	10.60 ± 0.04	0.31 ± 0.10	10.60 ± 0.04	10.70 ± 0.12	11.25 ± 0.19	10.89 ± 0.10
NGC 4388	10.67 ± 0.03	3.70 ± 0.11	10.57 ± 0.03	0.40 ± 0.10	10.74 ± 0.20	9.70 ± 0.13	10.38 ± 0.05	10.69 ± 0.03
NGC 4593	10.31 ± 0.02	1.70 ± 0.03	10.23 ± 0.02	0.47 ± 0.08	10.03 ± 0.01	10.67 ± 0.23	9.87 ± 0.04	10.37 ± 0.07
NGC 4602	10.49 ± 0.02	2.99 ± 0.07	10.48 ± 0.02	0.12 ± 0.31	10.12 ± 0.11	···	8.97 ± 0.24	<8.78
NGC 5135	11.23 ± 0.03	15.61 ± 1.87	11.19 ± 0.12	0.25 ± 0.04	10.72 ± 0.08	7.98 ± 0.44	10.51 ± 0.02	11.19 ± 0.16
NGC 5256	11.52 ± 0.03	31.72 ± 1.39	11.50 ± 0.04	0.14 ± 0.17	11.18 ± 0.17	9.59 ± 0.23	10.83 ± 0.03	11.83 ± 0.25
NGC 5347	9.96 ± 0.01	0.71 ± 0.01	9.85 ± 0.01	0.53 ± 0.04	10.35 ± 0.30	8.67 ± 0.27	9.49 ± 0.18	9.43 ± 0.19
NGC 5506	10.45 ± 0.02	1.96 ± 0.08	10.29 ± 0.04	0.65 ± 0.07	10.63 ± 0.07	10.83 ± 0.15	10.38 ± 0.03	10.99 ± 0.12
NGC 5548	10.62 ± 0.03	2.10 ± 0.10	10.32 ± 0.05	0.72 ± 0.05	11.35 ± 0.02	11.52 ± 0.19	10.78 ± 0.07	10.64 ± 0.09

Table 3 – *continued*

Name	log(L_{IR})	SFR	log(L_{IR}^{SF})	f_{AGN}(5–40)	log(L_{bol}^{AGN})			
					IR	X-ray	[Ne V]	[O IV]
	log($L_\odot$)	$M_\odot$ yr^{-1}	log($L_\odot$)		log($L_\odot$)			
NGC 5953	10.41 ± 0.04	2.56 ± 0.10	10.41 ± 0.04	0.02 ± 0.60	8.87 ± 0.30	···	9.42 ± 0.06	9.84 ± 0.14
NGC 5995	11.33 ± 0.03	19.19 ± 2.30	11.28 ± 0.12	0.34 ± 0.05	11.32 ± 0.02	···	11.25 ± 0.05	10.87 ± 0.03
NGC 6810	10.68 ± 0.03	4.62 ± 0.55	10.66 ± 0.12	0.13 ± 0.52	10.02 ± 0.25	7.07 ± 0.46	<8.95	8.67 ± 0.28
NGC 6860	10.41 ± 0.03	2.02 ± 0.12	10.30 ± 0.06	0.49 ± 0.05	10.26 ± 0.06	10.51 ± 0.14	10.22 ± 0.01	10.23 ± 0.01
NGC 6890	10.33 ± 0.01	2.05 ± 0.25	10.31 ± 0.12	0.13 ± 0.69	9.73 ± 0.57	8.12 ± 0.27	9.87 ± 0.01	9.42 ± 0.09
NGC 7130[a]	11.32 ± 0.00	20.93 ± 0.05	11.32 ± 0.01	···	···	7.89 ± 0.01	10.89 ± 0.01	10.54 ± 0.01
NGC 7213	10.08 ± 0.03	1.01 ± 0.12	10.01 ± 0.12	0.44 ± 0.01	9.72 ± 0.02	9.85 ± 0.08	<8.92	<9.20
NGC 7469	11.65 ± 0.03	44.55 ± 5.35	11.65 ± 0.12	0.05 ± 0.60	10.93 ± 0.41	10.94 ± 0.12	11.24 ± 0.12	10.60 ± 0.03
NGC 7496	10.19 ± 0.03	1.55 ± 0.19	10.19 ± 0.12	···	···	···	<8.82	<8.27
NGC 7603	11.08 ± 0.02	8.84 ± 0.26	10.95 ± 0.03	0.55 ± 0.06	11.50 ± 0.02	···	<10.22	10.28 ± 0.20
NGC 7674	11.53 ± 0.03	23.58 ± 2.83	11.37 ± 0.12	0.58 ± 0.60	11.73 ± 0.30	···	12.04 ± 0.17	11.71 ± 0.11
TOLOLO 1238−364	10.83 ± 0.01	5.76 ± 0.17	10.76 ± 0.03	0.32 ± 0.60	10.60 ± 0.30	···	10.73 ± 0.06	10.30 ± 0.04
UGC 05101	11.91 ± 0.01	55.21 ± 6.63	11.74 ± 0.12	0.65 ± 0.03	12.04 ± 0.13	8.73 ± 0.54	11.28 ± 0.09	11.07 ± 0.11
UGC 07064	11.19 ± 0.01	15.22 ± 0.04	11.18 ± 0.01	0.12 ± 0.35	10.42 ± 0.34	···	11.02 ± 0.17	10.90 ± 0.14

[a]For this source, we do not find evidence of the presence of an AGN from the SED-fitting analysis. However, the detection of mid-IR lines as [Ne V] and [O IV] in the mid/far-IR spectra (see Table 1), and a recent analysis of the X-ray data including new *NuSTAR* data, indicate the possible presence of a heavily buried, Compton-thick AGN (Pozzi et al. in preparation).

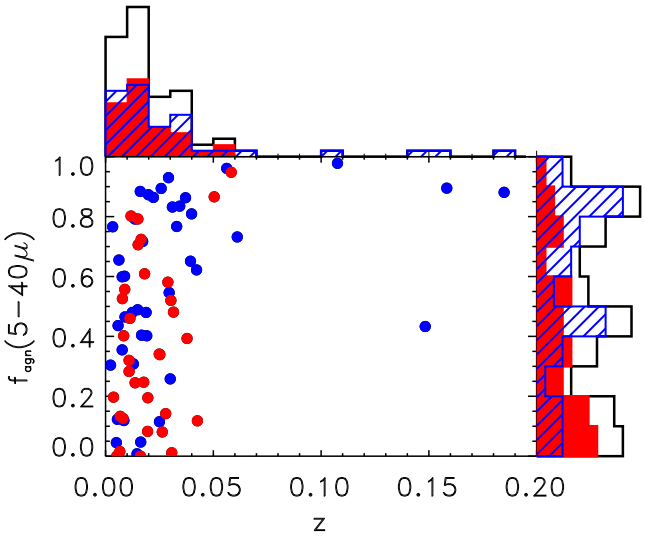

Figure 4. Left: fraction of luminosity due to the AGN in the 5–40 μm range versus redshift for Seyfert 1 (blue filled circles) and Seyfert 2 (red filled circles) from optical classification. The histograms on the top and right of the diagram represent the redshift and AGN fraction distributions respectively: total (black solid), Seyfert 1 (blue hatched) and Seyfert 2 (red filled).

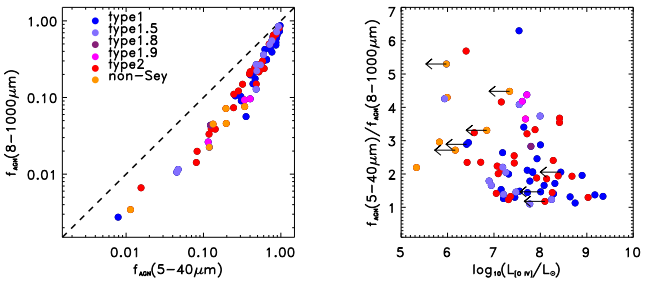

Figure 5. Left: fraction of luminosity due to the AGN in the 5–40 μm range against that in the 8–1000 μm range. The dashed line shows the 1–1 relation. Right: ratio between the fraction of luminosity due to the AGN in the 5–40 μm range and that in the 8–1000 μm range, versus the [O IV] 25.9 μm luminosity. The different types of galaxies – i.e. Seyfert 1/1.5/1.8/1.9/2 and non-Seyfert (i.e. H II regions and LINERs), as defined through optical spectroscopy (see Brightman & Nandra 2011b) – are shown by different colours, as explained in the legend.

2012; Lanzuisi et al. in preparation). Our sample is local, therefore we can compare our result with those found in the local Universe (Netzer et al. 2007; Netzer 2009): indeed a broad correlation is observed in our data between L_{IR}^{SF} and L_{bol}^{AGN}, with a slope similar to 0.8 and a scatter of ∼0.6 around the relation. However, as clearly noticeable from the colour gradient of the symbols in Fig. 7, if we divide the sample in subsamples with similar AGN fractions, the relation narrows significantly (scatter around the relation: ∼0.35 for f_{AGN}(5–40) < 30 per cent, ∼0.28 for 30 per cent < f_{AGN}(5–40) < 70 per cent, ∼0.30 for f_{AGN}(5–40) > 70 per cent), while the normalization increases with decreasing f_{AGN}(5–40) (e.g. sources with higher AGN fractions show lower SF luminosity at fixed AGN bolometric luminosities), although the slope for different intervals of AGN contribution keeps similar to that found by Netzer et al. (2007) for local AGN samples.

Indeed, if we calculate the Spearman's partial rank correlation coefficient for this correlation (to derive the significance, independent on redshift), we find that L_{IR}^{SF} and L_{bol}^{AGN} for the whole sample are loosely correlated (significance ∼1 σ), while the correlation becomes significant (at $\gtrsim 3\sigma$ level) if we divide the sources according to their AGN fraction (i.e. intervals of f_{AGN} discussed above). These results imply that at fixed SF luminosity, sources with higher AGN luminosity have also higher AGN contribution in the mid-IR. On the other hand, at a fixed AGN fraction, the AGN luminosity closely correlates with the SF luminosity, with apparently no dependence on luminosity (i.e. the correlation holds for low- and high-luminosity sources).

Recently, Theios, Malkan & Ross (in preparation) decomposed the H α luminosity of a representative sample of the 12MGS Seyferts into $L_{H\alpha}^{SF}$ and $L_{H\alpha}^{AGN}$ by means of narrow band filter imaging, also finding a correlation between the two quantities, not entirely due to selection effects. The correlation is different for Seyfert 1 and Seyfert 1.9/2: Seyfert 1s show greater nuclear H α luminosities, due to the presence of broad-line regions.

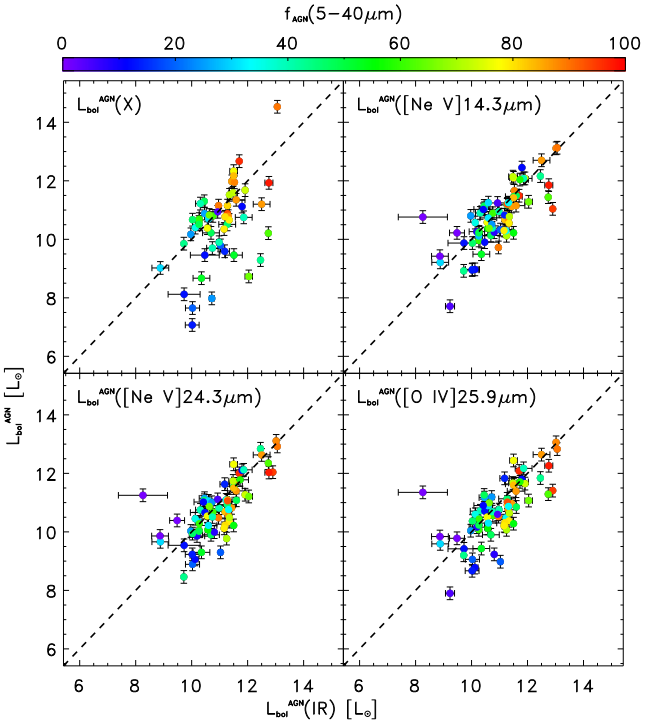

Figure 6. AGN bolometric luminosity obtained from the best-fitting torus model versus the AGN bolometric luminosity derived from different indicators: top left: X-ray (2–10 keV) luminosity; top right: [Ne V] 14.3 μm emission line; bottom left: [Ne V] 24.3 μm emission line; bottom right: [O IV] 25.9 μm line. The symbols shown in colour gradient represent sources with different fractions of the luminosity produced by the AGN in the 5–40 μm wavelength range, as shown in the top. The dashed line represents the 1–1 relation.

Our result confirms previous ones for local AGN, showing that in the local Universe the SF and accretion luminosities are intimately connected. They might also reflect a relation between $f_{\rm AGN}$(5–40) and $L_{\rm IR}^{\rm SF}/L_{\rm bol}^{\rm AGN}$, so that galaxies with higher AGN fraction tend to have higher AGN luminosities for a given $L_{\rm IR}^{SF}$. Hints of SF luminosity independent on the accretion one, i.e. the 'SF-dominated' regime, are apparently observed for few galaxies with very low AGN contribution ($f_{\rm AGN} \lesssim 5$ per cent).

5 AGN/SB DIAGNOSTICS

IR lines can be excited primarily by SF, by an AGN or by both. The typical AGN lines are three ([Ne V] 14.3 μm, [Ne V] 24.3 μm and [O IV] 25.9 μm), while the lines and features that are mainly produced in star-forming regions are: PAH 6.2 μm, PAH 11.2 μm, [Ne II] 12.8 μm, [S III] 18.7 μm, [S III] 33.5 μm, [Si II] 34.5 μm, [O I] 63 μm, [N II] 121.9 μm, [O I] 145.5 μm, and [C II] 157.7 μm. The other lines from [S IV] 10.5 μm, [Ne III] 15.5 μm, [O III] 52 μm, [N III] 57 μm and [O III] 88 μm, are excited by both AGN and newly born stars. All these lines cover a wide parameter space of the critical density versus ionization potential diagram, tracing different astrophysical conditions: from PDRs, to stellar/H II regions, to the AGN, and coronal line regions (Spinoglio & Malkan 1992). This makes the combination of their ratios very useful for the definition of AGNs versus SF diagnostic diagrams (e.g. Spinoglio & Malkan 1992; Genzel et al. 1998; Smith et al. 2007b). Higher ionization lines (i.e. [Ne III] 15.5 μm, [O IV] 25.9 μm, [O III] at 52 and 88 μm and [N III] 57 μm) are excited in H II regions, but can be excited also in AGN narrow-line regions (NLR) with typical conditions (e.g. high densities and ionization potentials). Therefore, in composite objects (like the great majority of our Seyfert galaxies, containing both an SF and an AGN component), the total line emission is the sum of the two components. The two [Ne V] lines at 14.3 and 24.3 μm are exclusively excited by AGN and can be considered AGN spectral signatures (e.g. Tommasin et al. 2010), while the [O IV] 25.9 μm line is at least a factor of 10 brighter, with respect to the continuum, in AGN than in starburst galaxies (e.g. Pereira-Santaella et al. 2010).

One of our aims is to test and calibrate our results in terms of accretion luminosity and AGN fractions using mid- and far-IR spectral features. First, we test the diagnostic diagrams commonly used in the literature to estimate the AGN contribution (e.g. through the [Ne V] to [Ne II] line ratio) and the SF contribution (e.g. with the EWs of the 11.25 μm PAH feature). In fact, since [Ne V] 14.3 μm and [O IV] 25.9 μm are the best AGN tracers in the *Spitzer*-IRS spectral range, their normalization to the [Ne II] 12.8 μm (mainly produced in the H II/SF regions), can provide ionization-sensitive ratios with all the sources (type 1s and type 2s) lying along the same sequence, as extensively discussed by Tommasin et al. (2010). This diagram can be used to estimate the ionizing power in the NLR, both in type 1 and 2 AGN. Therefore, the clear positive correlation represents an excitation sequence anchored with the H II/LINERs, moving up in excitation level to the Seyfert 2s and Seyfert 1s, and ending with the PG QSOs (Veilleux et al. 2009). Pereira-Santaella et al. (2010) used the photoionization code MAPPINGSIII (Groves, Dopita & Sutherland 2004) to interpret some of the AGN line ratios considered in this figure, finding basically no differences between type 1 and type 2 AGN.

In Fig. 8, we show the line ratios [Ne V] 14.3 μm/[Ne II] 12.8 μm (*top-left* panel), [O IV]25.9 μm/[Ne II]12.8 μm (*top right*), [Ne V] 14.3 μm/[Si II] 34.8 μm (*bottom left*) and [Ne III]15.5 μm/[Ne II] 12.8 μm (*bottom right*) as a function of the EW of the PAH feature at 11.25 μm. The *top* and *bottom* diagrams show the same line ratios as reported in figs 4 and 5 of Tommasin et al. (2010), although the AGN in that work were classified based on mid-IR line diagnostics. Our classification based on SED decomposition seems to agree well with the previous ones, with all the objects with high AGN fraction (e.g. >70 per cent) showing an absolute value of the EW of the PAH at 11.25 μm <0.1 μm and a neon ratio [Ne V]/[Ne II] > 0.1. On the other hand, most of the objects with low $f_{\rm AGN}$ (e.g. <30 per cent) have |EW PAH| > 0.1 μm and [Ne V]/[Ne II] < 0.5. The diagrams PAH EW versus [O IV]/[Ne II], [Ne V]/[Si II] and [Ne III]/[Ne II] show similar characteristics as the previous one: the line ratio (and the AGN fraction) increases when the absolute value of the PAH EW decreases. All these diagrams show the general inverse relation between the AGN dominance, as measured from the SED fitting and the ionization sensitive line ratios, and the SF dominance, estimated from the PAH EW. We note that the strong PAH emission detected in the spectra of low- and high-z samples of AGN (e.g. Lutz et al. 2008; Hanami et al. 2012; Castro et al. 2014; Alonso-Herrero et al. 2014), providing evidence for intense SF in the hosts of these sources, are not in contrast with our result, that show basically no feature for sources AGN-dominated in the 5–40 μm range, not depending on the strength of the central AGN.

Fig. 9 shows different diagnostics using mid- and far-IR line ratios and/or far-IR luminosity/flux, commonly used in the literature to segregate AGN-dominated sources from SF-dominated ones: [O IV] 25.9 μm/[Ne II] 12.8 μm versus [Ne V] 14.3 μm/[Ne II] 12.8 μm (*top left*), [O IV] 25.9 μm/FIR (*top right*) versus $L_{\rm IR}$, [C II] 158 μm/[O I] 63 μm versus [O III]88 μm/[O IV] 25.9 μm line ratio (*bottom left*)

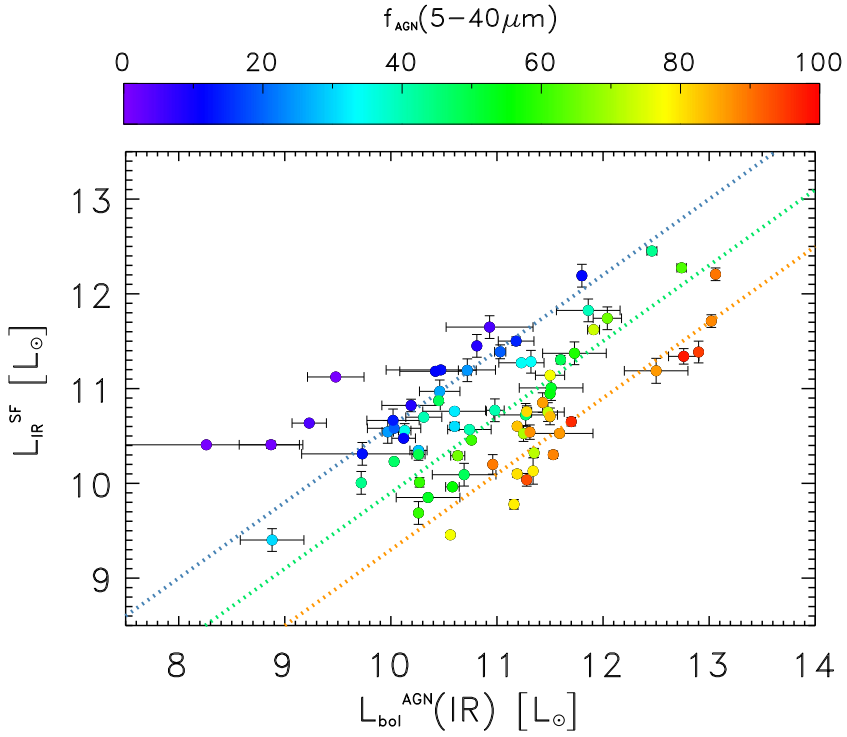

Figure 7. IR luminosity due to SF ($L_{\rm IR}^{\rm SF}$) versus AGN bolometric luminosity ($L_{\rm bol}^{\rm AGN}(IR)$) for different fractions of AGN contribution to the 5–40 μm luminosity (defined by the different colour gradient, as shown in the top). The three dotted lines are the best fit to data with different $f_{\rm AGN}$(5–40 μm), keeping fixed the slope of the relation at the same value found by Netzer et al. (2007) for local AGN: $L_{\rm SF} \propto L_{\rm bol}^{0.8}$ (>70 per cent orange, 30–70 per cent green, <30 per cent blue).

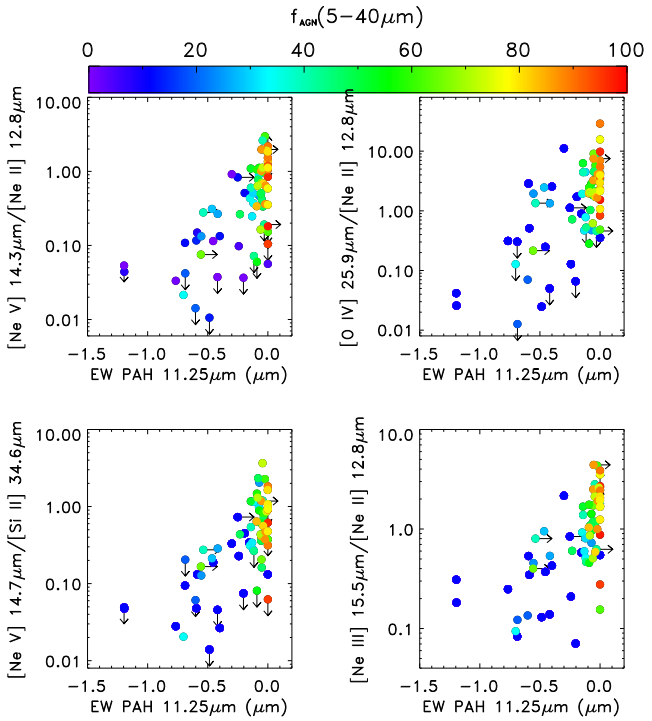

Figure 8. Mid-IR line ratios versus the PAH 11.25-μm EW (the top and bottom panels show the same diagnostics as reported in figs 4 and 5 of Tommasin et al. 2010, respectively). As in Fig. 6 and as shown in the colour bar on top, the different colours of the symbols represent different fractions of AGN contribution to the 5–40 μm luminosity.

and [C II]158 μm+[O I] 63 μm versus ([C II] 158 μm+[O I] 63 μm) / $L_{\rm FIR}$ (*bottom right*). As in the previous figure, the ionization-sensitive ratios ([O IV]/[Ne II] and [Ne V]/[Ne II]) show higher values for sources with higher AGN fractions.

The diagnostic shown in the *upper-right* panel is commonly used to estimate the level of contamination due to SF in the [O IV] line (or, rather, the sources for which an AGN is needed to explain the [O IV] emission): the higher [O IV]/FIR ratios shown by our AGN-dominated sources are consistent with our expectations based on previous results (e.g. Sturm et al. 2010; Graciá-Carpio et al. 2011).

As discussed also by Spinoglio et al. (2015), the [C II]158 μm / [O I] 63 μm versus the [O III] 88 μm/[O IV] 25.9 μm line ratio (see *bottom-left* panel), although the 12MGS sources with measured far-IR lines are just few, is able to separate AGN-dominated sources from SF dominated ones (in particular, the [O III]/[O IV] ratio). The [C II]/[O I] line ratio is only weakly able to segregate sources with different fractions of AGN, although we observe on average lower ratio values for AGN-dominated objects.

The *bottom-right* panel shows the [C II] 158 μm/[O I] 63 μm versus ([C II] 158 μm+[O I] 63 μm)/FIR diagram: sources with higher AGN fractions are located preferentially at lower [C II]/[O I] ratio values and at higher ([C II]+[O I])/FIR values. [O I] and [C II] are the brightest cooling lines of the cool ISM in galaxies. However, *ISO* showed the [C II] line in local Ultra Luminous Infrared Galaxies (ULIRGs, LIR > 10^{12} $L_{\odot}$) to be about an order of magnitude lower relative to the FIR continuum than in normal and starburst galaxies (e.g. Malhotra et al. 2001; Luhman et al. 2003). The [C II]/[O I] ratio is known to be sensitive to gas density in star-forming galaxies (e.g. Genzel & Cesarsky 2000), with the ratio decreasing with increasing density (PDRs account for more than half of the [C II] emission in starburst galaxies, while strong shocks could boost

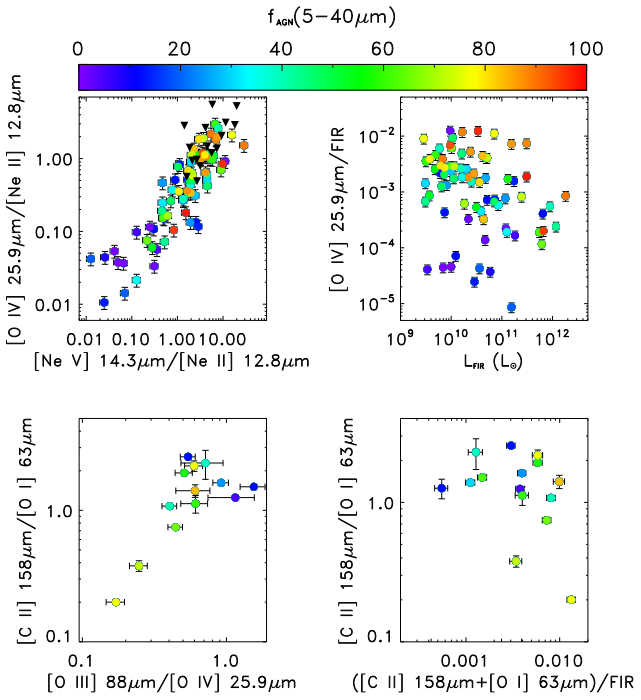

Figure 9. Mid-/far-IR line diagnostics commonly used to separate AGN from SF powered sources. As in the previous figures and as shown in the top colour bar, the different colours of the symbols represent different fractions of the AGN contribution to the 5–40 μm luminosity, as derived from our SED-fitting decomposition. The black filled triangles in the top-left panel show, for comparison, the location of the Palomar Green (PG) QSOs in the [O IV]/[Ne II] versus [Ne V]/[Ne II] plane (Schweitzer et al. 2006).

the [O I] emission relative to [C II]), while the larger values of the ([C II]+[O I])/FIR ratio shown by our AGN-dominated sources imply normal values and not a deficit in the major PDR cooling lines relative to the FIR. A detailed discussion on the line ratios characteristics and sensitivity to ionization and density is given by Spinoglio et al. (2015), but it is far from the scope of this work: here we plot these diagnostics uniquely with the aim of checking our decomposition results and their reliability (in particular to verify that objects with different AGN fractions are located where expected). Indeed, we see a trend in our data, in all panels and figures, with AGN-to-SF-dominated line ratios increasing with increasing AGN fraction.

6 LINE–LUMINOSITY RELATIONS

We find that the luminosities of the mid-/far-IR lines of our 12MGS subsample correlate with both the total IR luminosity due to SF ($L_{\rm IR}^{\rm SF}$) and the bolometric luminosity of the AGN ($L_{\rm bol}^{\rm AGN}$). The best-fitting parameters (the intercept and slope constants) of the linear relations (on a log–log scale) and their associated probable uncertainties have been derived by minimizing the chi-square error statistic, considering the data errors on both axes. In Fig. 10, we plot the mid-IR line luminosity versus the total IR luminosity due to SF (*left-hand* panels) and versus the AGN bolometric luminosity (*right-hand* panels), as derived from the SED decomposition (Section 4). The linear relations best fitting the data are reported, together with their intrinsic scatter (grey regions around the relations). Note that the intrinsic scatter considered here represents the dispersion, σ, given by the rms deviation of the data from the mean relationship, obtained by considering a Gaussian distribution around the mean (see Bonato et al. 2014a,b). Therefore, the shaded bands shown in the plots represent the $\pm1\sigma$ uncertainty regions that we need to take into account when we derive the line LFs by converting the total IR/AGN LFs using these relations (see next section). The relations between the (fewer) far-IR line and $L_{\rm IR}^{\rm SF}$ (*left*) and $L_{\rm bol}^{\rm AGN}$ (*right*) luminosities are shown in Fig. 11, with their intrinsic scatter as in the previous figure. We stress that, although for some lines and sources there are upper limits, they are available not for all the considered lines (e.g. the collection of data is not always uniform), having just no data or no observation in some cases (mainly for the far-IR lines, but also for some mid-IR ones). Therefore, for homogeneity, we decided not to consider any upper limits in our analysis, but only detections, although when available, we plot the limits as pointing-down arrows in the figures.

From the *left-hand* panels of Fig. 10, we note that for the SF-dominated lines (i.e. PAHs, [Ne II], etc.), a unique relation is derived between the line and the SF luminosity, regardless of the AGN fraction; while for the AGN-dominated lines (i.e. [Ne V], [O IV], etc.), the relation changes as the AGN fraction increases. In particular, by dividing the sample in two (according to $f_{\rm AGN}$(5–40 μm)> and <40 per cent), we find that galaxies in the higher $f_{\rm AGN}$ subsample show higher (AGN-dominated) line luminosity at a given SF luminosity. These results are confirmed by the location of the PG QSOs (AGN-dominated) in some of these diagrams (shown for comparison as black filled triangles), as derived by Schweitzer et al. (2006): they always occupy the same region of our sources with higher AGN fraction (i.e. are at higher line luminosities in the [Ne V] and [O IV] versus SF luminosity diagrams and mixed up with the other sources regardless the AGN fraction in the [Ne II] versus SF luminosity one). The opposite happens to the relation between the line luminosity and the AGN bolometric luminosity (see the *right-hand* panels of Fig. 10): at a given $L_{\rm bol}^{\rm AGN}$, sources with higher AGN fraction show lower (SF-dominated) line luminosity, but the same line luminosity if the lines are AGN-dominated (just one correlation, regardless their $f_{\rm AGN}$). This reflects the fact that lines mostly excited by SF have a major contribution not related to the AGN, with their luminosity enhanced for higher SF fraction (lower AGN fraction) with respect to sources with similar AGN luminosity, but lower SF fraction (higher AGN one). The significance level associated with these luminosity–luminosity correlations, independent on redshift, is derived through the Spearman partial rank correlation coefficients (Macklin 1982). We find a high significance for the correlations between all the mid-IR lines and the IR luminosity due to SF (between $\sim$3 and 7σ) and between the AGN mid-IR lines (i.e. [Ne V], [Ne III] and [O IV]) and the AGN bolometric luminosity (at $\gtrsim3.5\sigma$). Instead, the significance is lower between SF-dominated lines and AGN bolometric luminosity (between $\sim1\sigma$ and $\sim2\sigma$), but increases to 2.5σ–5σ for the subsamples defined according to $f_{\rm AGN}$(5–40μm)< or >40 per cent.

Note that, since a measure of the far-IR lines are available only for a limited number of sources, the results (in terms of linear coefficients and significance) obtained by dividing the sample in two (according to the $f_{\rm AGN}$(5–40 μm)< or >40 per cent criterion) are not wholly meaningful, given the very large uncertainties. However, the trend of sources with higher AGN fraction showing brighter IR lines (due to SF) found for the mid-IR lines (more numerous and statistically significant sample) is confirmed also for the far-IR lines.

The best-fitting parameters and their probable uncertainties found for the different line–luminosity relations, expressed in the form

$$\log_{10}(L_{\rm line}) = a \cdot \log_{10}(L_{\rm IR}) + b \qquad (1)$$

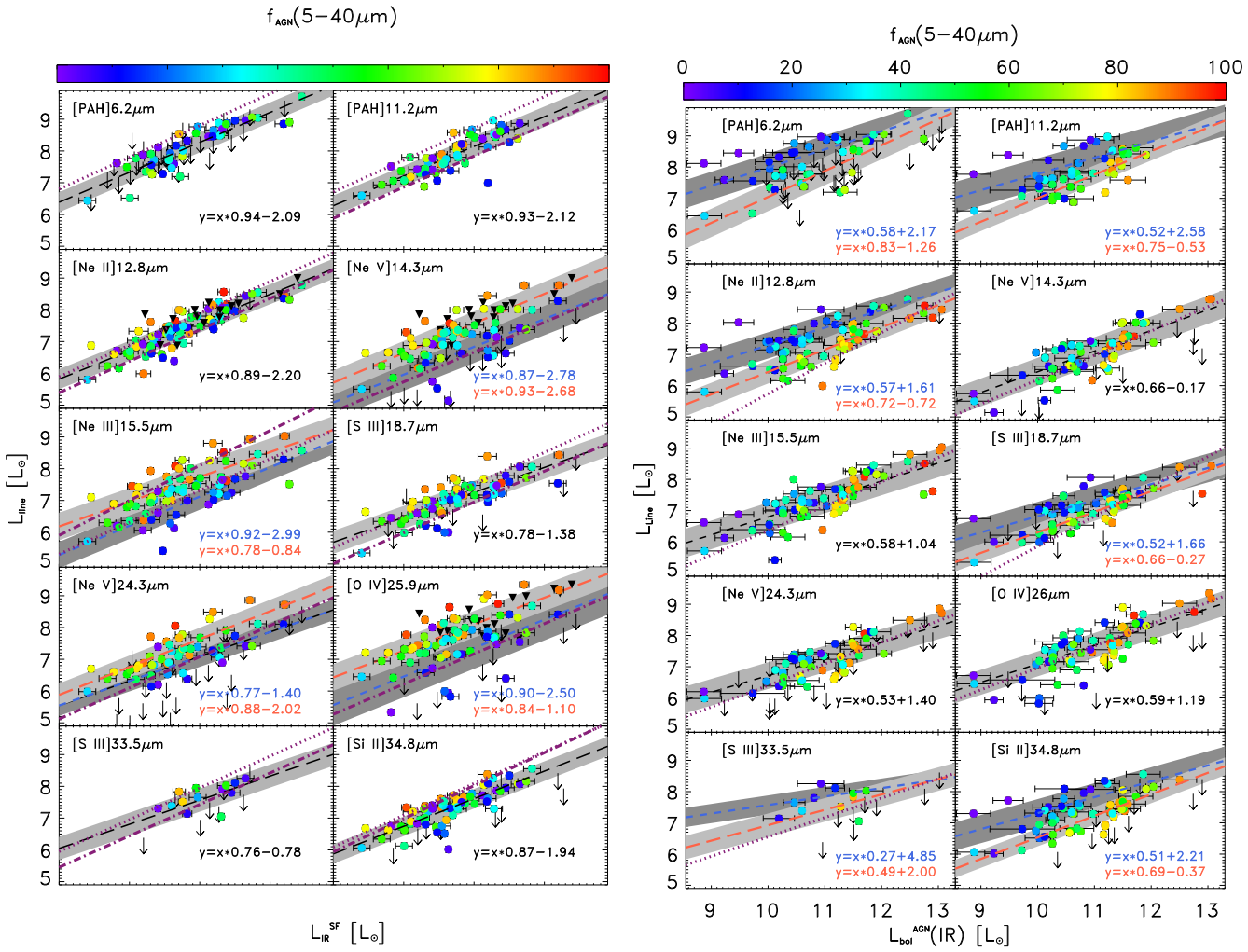

Figure 10. Luminosity of the different mid-IR lines as a function of the 8–1000 μm luminosity due to SF ($L_{\rm IR}^{\rm SF}$, left-hand panels) and of the AGN bolometric luminosity ($L_{\rm bol}^{\rm AGN}$(IR), right-hand panels) derived from our SED fit. The different colours of the symbols, as well as in the previous figures, represent the different AGN fractions to the 5–40 μm luminosity derived through our SED decomposition analysis. For comparison, values relative to the PG QSOs, as derived by Schweitzer et al. (2006), are shown as black filled triangles in the left-hand panels (for the available lines and assuming that $L_{\rm IR}^{\rm SF} \sim L_{60\,\mu\rm m}$). The long-dashed orange and the short-dashed blue lines show the best-fitting relations found for sources with a 5–40μm AGN fraction larger and smaller than 40 per cent, respectively (the light and dark grey areas are the relative intrinsic dispersion). For lines showing a unique relation regardless of the AGN fraction, the long-dashed black line (within the grey area) shows the 'global' best-fitting relation (with its intrinsic dispersion). The purple dotted and dot–dashed lines represent the best-fitting relations found by (Bonato et al. 2014a,b) and Spinoglio et al. (2012), respectively. Upper limits are shown by downward pointing arrows.

$$\log_{10}(L_{\rm line}) = c \cdot \log_{10}(L_{\rm bol}^{\rm AGN}) + d \quad (2)$$

$$\log_{10}(L_{\rm line}) = e \cdot \log_{10}(L_{\rm IR}^{\rm SF}) + f \quad (3)$$

are listed in Table 4.

7 THE LINE LFs

Our understanding of the cosmological evolution of IR sources has dramatically improved in recent years, but studying the co-evolution of SF and black hole accretion is still one of main scientific goals of the future astrophysical missions, both in the X-rays and in the IR. Observational determinations of the evolution of the IR population up to $z \simeq 4$ are now available, thanks to *Herschel* (e.g. Gruppioni et al. 2013), although the major step forward will be the characterization and the evolution with redshift of their physical properties. This will be possible only through IR spectroscopy, provided by planned or forthcoming facilities, like, e.g. *JWST* and *SPICA*, that will explore the distant Universe in the near-/mid-IR and mid-/far-IR, respectively. In order to understand what will be spectroscopically observable for galaxies and AGN, we need to estimate the redshift and galaxy luminosity ranges that can be measured, based on the line LFs. A key ingredient to make such estimates is the relationship between the line and the total IR (or SF/AGN) luminosity, that will allow us to rely on the evolution of the IR (SF/accretion) LF: to this purpose, we use the ratios obtained in the previous section, between the line luminosity and the total IR (SF/AGN) luminosity, to derive the mid-/far-IR line LFs.

Note that, converting the accretion LFs (e.g. Hopkins, Richards & Hernquist 2007; Delvecchio et al. 2014) using the relations found between the line luminosity and the AGN accretion luminosity, and the SFR LFs (e.g. Gruppioni et al. 2015) is probably the most appropriated approach for the AGN-dominated lines (or for objects containing an AGN, at any level of dominance) and the SF-dominated

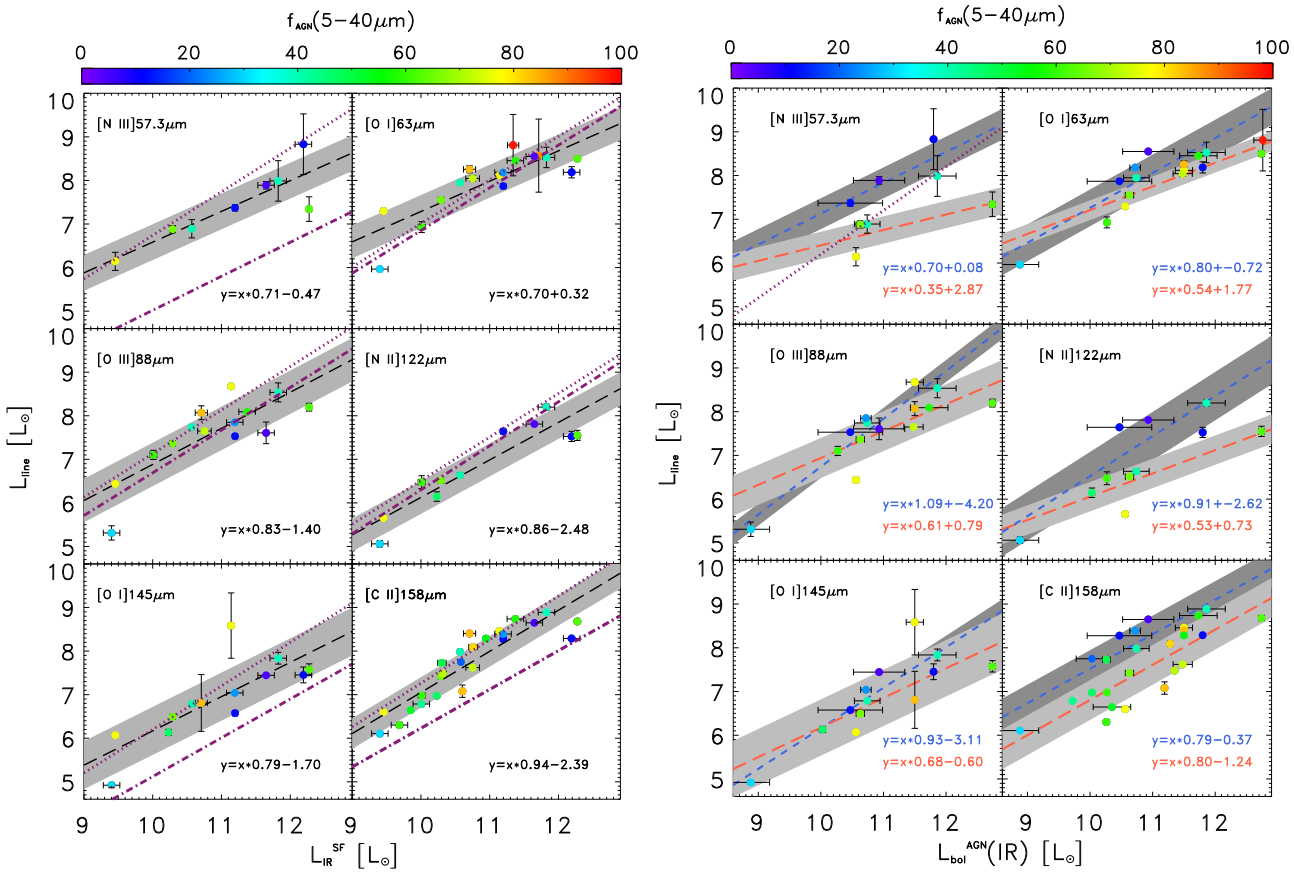

Figure 11. Luminosity of the different far-IR lines as a function of the 8–1000 μm luminosity due to SF ($L_{\rm IR}^{\rm SF}$, left-hand panels) and of the AGN bolometric luminosity ($L_{\rm bol}^{\rm AGN}$(IR), right-hand panels) derived from our SED fit. As in the previous figures, the different colours of the symbols represent the different 5–40 μm AGN fractions (see top colour bar). The long-dashed black line (within the grey area) shows the best-fitting relation (with its intrinsic dispersion), while the long-dashed orange and the short-dashed blue lines in the right-hand panels show the best-fitting relations found for sources with a 5–40 μm AGN fraction larger and smaller than 40 per cent, respectively (the light and dark grey areas are the relative intrinsic dispersion). The purple dotted and dot–dashed lines represent the best-fitting relations found by Bonato et al. (2014a,b) and Spinoglio et al. (2012), respectively.

ones, respectively. However, the AGN bolometric luminosity and the SFR depend on several assumptions: the former, i.e. on the bolometric correction, needed whatever the AGN selection would be, which depends on the observing band and – strongly – on the considered AGN model; the latter on the stellar population synthesis models, their SF histories, etc. For this reason, they are not quantities directly measurable by the observations as, instead, is the total IR luminosity (very robust if far-IR data are available). Therefore, here we decide to use the total IR LF (and the line – total IR luminosity relations: e.g. coefficient a and b in Table 4) instead of the SFR or accretion LFs, since the adopted approach is more direct and applicable to virtually any galaxy samples observed in the IR, for which a measure of the total IR LF is available. As a quality test, we have also followed the other approach, converting the AGN bolometric LFs derived by Delvecchio et al. (2014) into line LFs through the line–AGN luminosity relations (coefficient c and d in Table 4) for the AGN-dominated lines ([Ne V], [Ne III], [O IV]), and the SFR LFs by Gruppioni et al. (2015) and the line–SF luminosity relations (coefficient e and f in Table 4) for the other lines (SF-dominated). The line LFs derived with this second approach are well consistent (e.g. within 1 σ) with those obtained by converting the total IR LF.

The line LFs can be easily computed from the total IR ones by convolving the latter with the distribution of the IR-to-line luminosity ratios, assumed to be a Gaussian with mean value given by the best-fitting relations and standard deviation equal to the intrinsic dispersion (which must be added to the data errors to obtain the total uncertainty in the relations). The detailed LF analysis performed by Gruppioni et al. (2013) and the evolutions found for the different populations, allow us to convert the total IR LF not 'globally', with an average relation, but considering the *Herschel* populations separately by using the line-to-total IR luminosity relations corresponding to their median AGN fraction (in the 5–40 μm range, as derived by Delvecchio et al. 2014 through an accurate SED decomposition). We therefore convert the total IR LFs applying the appropriate relation to each population of IR objects observed by *Herschel*, given the average AGN fraction of that population. In particular, Gruppioni et al. (2013) divided the IR population in five main classes, based on their broad-band SEDs: `spiral`, `starburst`, `SF-AGN` (sub-divided into `SF-AGN(Spiral)` and `SF-AGN(SB)` as they represent low-luminosity and obscured AGN, respectively), `AGN1` and `AGN2`. Successively, Delvecchio et al. (2014) performed an SED decomposition analysis (as the one performed in this work), deriving the AGN bolometric luminosity and the fraction of AGN luminosity in different wavelength ranges for each source considered by Gruppioni et al. (2013). Since the average $f_{\rm AGN}$(5–40) found for the `AGN1` and `AGN2` populations (e.g. those with AGN-dominated SEDs) is larger than 40 per cent, we have considered the relation

Table 4. Best-fitting parameters of the line–luminosity relations: $\log_{10}(L_{\rm line}) = a \cdot \log_{10}(L_{\rm IR}) + b$ [equation 1]; $\log_{10}(L_{\rm line}) = c \cdot \log_{10}(L_{\rm bol}^{\rm AGN}) + d$ [equation 2]; $\log_{10}(L_{\rm line}) = e \cdot \log_{10}(L_{\rm IR}^{\rm SF}) + f$ [equation 3].

Line	a	b	c	d	e	f	$f_{\rm AGN}$(5–40 μm)(%)
PAH 6.2	0.92 ± 0.02	−1.91 ± 0.27	0.58 ± 0.03	2.17 ± 0.29	0.94 ± 0.02	−2.09 ± 0.27	<40
			0.83 ± 0.03	−1.26 ± 0.37			>40
PAH 11.2	0.95 ± 0.03	−2.41 ± 0.31	0.52 ± 0.04	2.58 ± 0.30	0.93 ± 0.03	−2.12 ± 0.30	<40
			0.75 ± 0.04	−0.53 ± 0.40			>40
[Ne II] 12.8	0.87 ± 0.19	−2.17 ± 0.21	0.57 ± 0.02	1.61 ± 0.25	0.89 ± 0.019	−2.20 ± 0.21	<40
			0.72 ± 0.02	−0.72 ± 0.24			>40
[Ne V] 14.3	0.93 ± 0.04	−3.55 ± 0.40	0.58 ± 0.02	0.66 ± 0.25	0.91 ± 0.04	−3.34 ± 0.40	<40
	0.78 ± 0.02	−1.36 ± 0.25			0.77 ± 0.02	−1.08 ± 0.25	>40
[Ne III] 15.5	0.92 ± 0.04	−2.99 ± 0.40	0.52 ± 0.02	1.68 ± 0.25	0.92 ± 0.04	−2.99 ± 0.40	<40
	0.78 ± 0.02	−1.10 ± 0.25			0.78 ± 0.02	−0.84 ± 0.25	>40
[S III] 18.7	0.79 ± 0.02	−1.59 ± 0.22	0.52 ± 0.03	1.68 ± 0.25	0.78 ± 0.02	−1.38 ± 0.25	<40
			0.66 ± 0.03	−0.27 ± 0.28			>40
[Ne V] 24.3	0.80 ± 0.04	−1.95 ± 0.41	0.44 ± 0.03	2.48 ± 0.28	0.63 ± 0.03	−0.02 ± 0.36	<40
	0.90 ± 0.02	−2.69 ± 0.25			0.88 ± 0.02	−2.3 ± 0.26	>40
[O IV] 25.9	0.74 ± 0.04	−0.87 ± 0.40	0.59 ± 0.01	1.19 ± 0.16	0.72 ± 0.04	−0.66 ± 0.40	<40
	0.73 ± 0.02	−0.21 ± 0.25			0.70 ± 0.02	0.31 ± 0.25	>40
[S III] 33.5	0.72 ± 0.05	−0.53 ± 0.61	0.27 ± 0.05	4.85 ± 0.47	0.76 ± 0.06	−0.78 ± 0.66	<40
			0.49 ± 0.33	2.00 ± 3.79			>40
[Si II] 34.8	0.86 ± 0.02	−2.03 ± 0.23	0.51 ± 0.03	2.21 ± 0.27	0.87 ± 0.03	−1.94 ± 0.27	<40
			0.69 ± 0.03	−0.37 ± 0.34			>40
[N III] 57.3	0.71 ± 0.09	−0.67 ± 0.50	0.70 ± 0.09	0.08 ± 1.04	0.71 ± 0.04	−0.47 ± 0.46	<40
			0.35 ± 0.06	2.87 ± 0.67			>40
[O I] 63	0.72 ± 0.04	−0.08 ± 0.35	0.80 ± 0.04	−0.72 ± 0.48	0.70 ± 0.03	0.32 ± 0.35	<40
			0.54 ± 0.04	1.77 ± 0.41			>40
[O III] 88	0.88 ± 0.04	−2.11 ± 0.40	1.09 ± 0.05	−4.20 ± 0.53	0.82 ± 0.035	−1.40 ± 0.39	<40
			0.61 ± 0.05	0.79 ± 0.56			>40
[N II] 122	0.88 ± 0.04	−2.76 ± 0.37	0.91 ± 0.04	−2.62 ± 0.48	0.86 ± 0.03	−2.48 ± 0.36	<40
			0.53 ± 0.05	0.73 ± 0.54			>40
[O I] 145	0.84 ± 0.03	−2.38 ± 0.38	0.93 ± 0.04	−3.11 ± 0.48	0.79 ± 0.03	−1.70 ± 0.37	<40
			0.68 ± 0.05	−0.60 ± 0.55			>40
[C II] 158	0.96 ± 0.03	−2.73 ± 0.31	0.79 ± 0.04	−0.37 ± 0.46	0.94 ± 0.03	−2.39 ± 0.30	<40
			0.80 ± 0.03	−1.24 ± 0.38			>40

found for sources with an AGN contribution to the 5–40 μm luminosity larger than 40 per cent. For all the other populations (i.e. `spiral`, `starburst`, `SF-AGN(Spiral)` and `SF-AGN(SB)`), we have instead considered the relation for sources with less than 40 per cent of AGN (since their average $f_{\rm AGN}$(5–40) resulted lower).

Note that, since there is virtually no contribution of star-forming galaxies to the [Ne V] lines, we have not converted to [Ne V] LFs the total IR LFs of the two populations powered by SF (i.e. `spiral` and `starburst` galaxies), while for the [Ne III] 15.5 μm and [O IV] 25.9 μm lines we have derived (and applied to those two population LFs) a relation for the SF component only by using the pure starburst sample of Bernard-Salas et al. (2009). For all the other lines, we have considered the emission to be dominated by SF and we have applied the derived relations to all the lines (according to the different AGN fractions).

In Fig. 12, we show an example of line LF ([O IV] 25.9 μm), where the contributions of the different populations are highlighted by different colours (described in the legend) and the total contribution (sum of all the populations), with its uncertainty region (obtained by considering the intrinsic and measurement errors in the relations) being shown as grey filled area and compared to the result we would have obtained by applying to the total IR LF a 'global' average relation for all the populations (described by the a and b parameters in Table 4: black dashed line with uncertainty region defined by the hatched area).

We note that the LFs obtained by using the average relation for all the sources or different relations for different AGN fractions, are almost consistent within 2σ, although at $z < 2$ and $L_{[\rm O\,IV]} > 10^9\,{\rm L}_\odot$, the two LFs differ by more than 2σ (especially at $0.6 < z < 0.8$). The main difference in this particular case can be noticed at the bright end of the line LF, where the AGN populations, if treated separately with their specific line-to-total IR luminosity relation, give a major contribution, mainly at $z < 2$. A slight difference in the LF knee is also observed in the same range of redshift, with the 'globally' converted line LF showing a higher Φ^* and a lower L^* with respect to the LF obtained by summing the different population contributions. At $z > 2$, where AGN-dominated populations dominate the IR LFs (especially the bright end), the difference

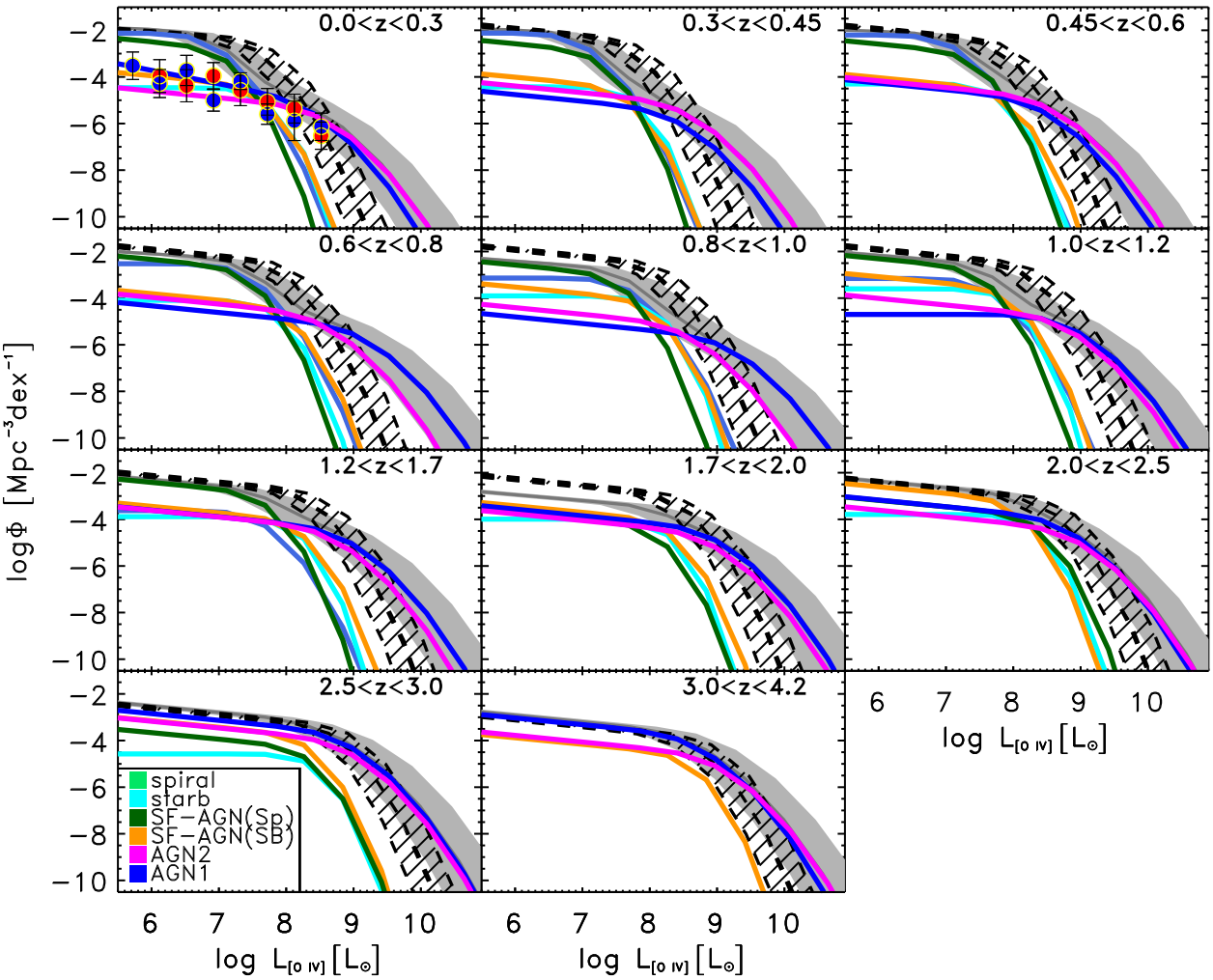

Figure 12. LF of the [O IV] 25.9 μm line in different redshift intervals, obtained by converting the total IR LF of Gruppioni et al. (2013) through the $L_{\rm line}$–$L_{\rm IR}$ relations found in Section 6. The different coloured lines represent the different IR populations (evolved and converted separately, according to their average AGN fraction), whose sum is shown by the grey band. The black dashed line shows the LF obtained by converting the total IR LF using the average $L_{[\rm O\,IV]}$–$L_{\rm IR}$ relation. The filled symbols in the $0.0 < z < 0.3$ panel show the [O IV] LF derived by Tommasin et al. (2010) for Seyfert 1 (red circles) and Seyfert 2 (blue circles) galaxies.

is negligible, since the average relation reflects the relation found for sources with high AGN fraction. For comparison, at the lower redshift ($0.0 < z < 0.3$) we have plotted also the values of the [O IV] LF found by Tommasin et al. (2010) for the Seyfert 1 and 2 of the 12MGS. The agreement with our estimates for `AGN1` and `AGN2+SF-AGN(SB)` is very good, although we stress that the faint end of our reference total IR LF for AGN-dominated objects (i.e. `AGN1` and `AGN2`) is not constrained at low redshift (e.g. the faint-end slope is taken from a higher z interval, more populated by AGN at low luminosities). The faint end of our derived [O IV] LF is dominated by low-luminosity AGN (`SF-AGN(GAL)`) and normal galaxies (`spiral`), which in principle should not be included in the 12MGS. Note that for lines mainly produced by SF, for which an average relation for all sources is found regardless of the AGN fraction (i.e. PAHs, [Ne II], [S III], [Si II] and all the far-IR lines; see Figs 10 and 11), the two approaches here described are equivalent.

For the sake of clarity, we note that the local relations found in this work – then applied to the *Herschel* populations up to high z to derive the evolution of the line LFs – are valid mainly at $L_{\rm line} < 10^9\,{\rm L}_\odot$, while the observed discrepancy occurs mainly at brighter luminosities. Unfortunately, at present, no data are available to constrain the local bright end of the line LFs. The purpose of this work (and section) is to present a method based on the best currently available data and models – improved with respect to the previous ones (see Section 3) – to provide expected numbers of detections in the different IR lines. All this will be crucial for planning spectroscopic surveys with the future facilities (see next section).

7.1 Predictions for future IR facilities

The line LFs obtained in the previous section provide an important tool to estimate how many sources will be observable in each of the considered mid-/far-IR lines with any forthcoming/future/planned/eventual facilities in the IR/sub-mm. With our LFs, we cannot only derive numbers, but redshift and luminosity distributions of the detectable sources to any flux limits, making it possible to plan future spectroscopic surveys in a crucial, but totally unexplored wavelength range for high-z sources.

In the next decades, a few space IR facilities will be put in orbit. Due to be launched in 2018, the *JWST* (Gardner et al. 2006) will be the next NASA observatory that will explore the Universe at near-/mid-IR wavelengths. The MIRI instrument (Wright et al. 2010) is the only mid-IR instrument for *JWST*, performing photometric imaging in between 5 and 27 μm over a 2.3 arcmin^2 field-of-view (FOV), and spectroscopy (including medium resolution, R ∼1500–3500, integral field spectroscopy over a 13 arcsec^2 FOV at 5–28.5 μm).

Complementary to *JWST*, *SPICA* (Nakagawa et al. 2012), to be proposed for the ESA 5th Medium missions call (due launch in 2028–2030), will observe the Universe at mid-/far-IR, from 10 to 37 μm with the SMI camera and spectrograph (Kataza et al. 2015) and continuously from 34 to 230 μm with the SAFARI grating spectrograph (Roelfsema et al. 2014). The *SPICA* 2.5-m diameter mirror, cooled down to $\lesssim$8 K, will allow us to reach unprecedented sensitivities over an unexplored wavelength range, bridging the gap between *JWST* and the Atacama Large Millimeter Array (ALMA). The resulting number of sources (per unit area) that will be detectable in each line as a function of z with the MIRI IFU spectrograph (by considering the nominal sensitivities) and *SPICA* (by considering the nominal sensitivities for the resolutions $R \sim$ 1300–2300 and $R \sim 300$ for SMI and SAFARI, respectively), to 5σ in 10 000 s (time on-source only) are presented in Table 5 and are plotted in the Fig. 13.

Figure clearly shows the complementarity of *JWST* and *SPICA*, the former being more efficient in detecting PAH features, but only the 6.2 μm one to high redshifts; the other mid-IR lines will run out of the MIRI range at much lower redshift, with [Ne V] 24.3 μm and [O IV] 25.9 μm being barely detectable up to $z < 0.1$–0.2. Similarly, the SMI contribution becomes less and less relevant for longer wavelength lines (such as [Ne V] 24.3 μm and above) and is more important at low redshifts, while SAFARI will allow us to detect mid-IR lines up to $z \sim$ 3–4. Note that, even for lines produced mainly by SF, objects containing an AGN provide a significant contribution (green and red coloured area in Fig. 13).

We must point out that the comparison between *JWST* and *SPICA* based on source numbers per unit area (depending only on sensitivity) is not totally realistic, it can only tell us the redshift ranges covered by the two missions. In order to discuss about the real efficiency of detecting sources in the different lines, we have to take into account the different FOV of the different instruments. Given its small FOV, MIRI will not be a survey instrument, however, it will be possible to perform very deep pencil-beam surveys over small areas of the sky. The slit length of SMI (medium resolution, $R \sim$ 1300–2300) on *SPICA* is planned to be 60 arcsec × 3.7 arcsec, while MIRI (medium resolution spectrograph, $R \sim 2400$) on *JWST* will have an FOV ranging from 3.6 arcsec × 3.6 arcsec to 7.6 arcsec × 7.6 arcsec from 6.4 to 22.5 μm. Therefore, within the same amount of time, SMI will scan an area of the sky ∼3.8 times larger than MIRI, even considering the longest wavelength band of the latter (with the larger FOV). As an example, in terms of observing time, to cover an area like the *HST* eXtreme Deep Field (10.8 arcmin^2) to the sensitivities considered in our simulations (5σ, 10 000 s on source), MIRI will have to observe ∼1800 h, against the ∼470 h of SMI. The SAFARI grating spectrograph will only make pointed observations of single sources at a time, therefore a direct comparison with the areal coverage of the mid-IR instruments is not possible. However, we have estimated that in ∼1000 h with SAFARI we will be able to observe (simultaneously over the whole 32–230 μm range) in at least three lines ∼20 $L_{\rm IR} \leq 10^{11}$ L$_\odot$ sources at $z \sim 1$, ∼20 $L_{\rm IR} \leq 10^{11.5}$ L$_\odot$ sources at $z \sim 2$ and ∼20 $L_{\rm IR} \leq 10^{12}$ L$_\odot$ sources at $z \sim 3$. These luminosities are below the knee of the IR LFs at the corresponding redshifts.

Note also that MIRI/*JWST* has spectroscopic coverage only up to 28 μm, and therefore most of the atomic and molecular diagnostic features will be inaccessible beyond $z \sim 2$. ALMA, which is designed for the sub-mm wavelengths, has coverage only beyond ∼330 μm and can be used to trace important far-IR fine-structure lines (e.g. [C II] 157 μm and [O III] 88 μm) at high redshift, but is blind to many of the mid-IR atomic, H_2 and dust features. *SPICA* will provide a unique window on the physical processes fuelling SF and BH growth in the dusty Universe.

8 CONCLUSIONS

We have exploited all the information – both photometric and spectroscopic, from X-rays to mm – available for 76 sources from the extensively studied 12MGS local sample of Seyfert galaxies, to perform a broad-band SED-fitting and decomposition and obtain new relations between mid- and far-IR line luminosity and AGN, SF and total IR luminosities, also investigating the variations of these relations for different fractions of AGN contribution. Thanks to the use of all the data available for these objects, we were able to derive crucial AGN and host galaxy quantities (i.e. the AGN bolometric luminosity, the AGN fraction in different wavelength ranges, the SFR) and greatly reduce the uncertainties and degeneracies with respect to similar SED-decomposition works performed at high-z, where the very few photometric points available in the mid-IR/far-IR range (crucial to constrain and separate the AGN and the starburst contributions) lead to very uncertain results. The relations found between the line luminosity and the SF or AGN or total IR luminosities, reflecting a connection between the black hole accretion and the SFR in the local AGN, are used to estimate numbers, redshifts and luminosities of sources detectable in the different mid-/far-IR lines.

The main results of this work can be summarized as follows.

(i) The observed broad-band SEDs of the 12MGS have been decomposed into three different components, peaking in three different regimes: evolved stars (optical/near-IR), dust-heated by SF (far-IR/sub-mm) and AGN dusty torus emission (mid-IR). Crucial physical quantities, as the SFR, the AGN bolometric luminosity, the total IR luminosity due either to SF or AGN, the AGN fraction in different wavelength ranges, are accurately derived, thanks to the wealth of data available, including IRS spectra in the mid-IR.

(ii) The 12MGS sources show all the range of AGN dominance in the mid-IR (e.g. 5–40 μm), from about 90 per cent to no AGN at all.

(iii) The AGN bolometric luminosity derived through the SED decomposition is in good agreement with previous derivations for the same objects from X-rays and high excitation mid-IR lines (i.e. [Ne V], [O IV]).

(iv) The SF luminosity is found to correlate nicely with the AGN bolometric luminosity, with the dispersion in the relation caused by the different fraction of AGN contribution to the IR luminosity: the normalization of the relation changes with $f_{\rm AGN}$, but the slope keeps similar to that found by Netzer et al. (2007, Netzer et al. 2009, e.g. sources with higher AGN fraction show lower SF luminosity at a given AGN bolometric luminosity).

(v) The total IR luminosity, the SF luminosity and the intrinsic AGN bolometric luminosity are found to correlate with the IR line luminosity. Variations of these relations with different AGN fractions are investigated resulting in higher AGN-line luminosities for sources with larger AGN fractions at given total IR luminosity, and

Table 5. Estimated redshift distributions (per unit area) of IR galaxies detectable by *JWST* and *SPICA* to 5σ with 10 000 s integration per FoV in each of the mid-IR emission lines. In parenthesis we give the number of detections of galaxies containing an AGN.

Spectral line	Instrument	0.01–0.3	0.30–0.45	0.45–0.6	0.6–0.8	0.8–1.0	1.0–1.2	1.2–1.7	1.7–2.0	2.0–2.5	2.5–3.0	3.0–4.2	All z
							(deg^{-2})						
PAH 6.2	MIRI	8(4)	1763(507)	2457(737)	2844(1534)	1651(1103)	2900(2244)	1888(1626)	468(365)	584(498)	282(268)	45(45)	14890(8931)
	SMI	0(0)	0(0)	0(0)	0(0)	0(0)	0(0)	0(0)	0(0)	338(280)	161(152)	23(23)	552(455)
	SAFARI	0(0)	0(0)	0(0)	0(0)	0(0)	0(0)	0(0)	0(0)	0(0)	0(0)	0(0)	0(0)
PAH 11.2	MIRI	8(4)	539(431)	1971(576)	2258(1177)	718(428)	1091(783)	638(525)	0(0)	0(0)	0(0)	0(0)	8223(3924)
	SMI	0(0)	0(0)	0(0)	731(344)	481(272)	668(462)	367(294)	126(92)	264(217)	0(0)	0(0)	2637(1682)
	SAFARI	0(0)	0(0)	0(0)	0(0)	0(0)	0(0)	0(0)	0(0)	0(0)	192(181)	36(36)	228(217)
[Ne II] 12.8	MIRI	8(4)	1107(294)	402(134)	412(187)	277(143)	315(204)	145(110)	0(0)	0(0)	0(0)	0(0)	2664(1076)
	SMI	0(0)	0(0)	183(69)	178(78)	130(60)	122(74)	51(37)	23(17)	0(0)	0(0)	0(0)	687(336)
	SAFARI	0(0)	0(0)	0(0)	0(0)	0(0)	0(0)	0(0)	57(41)	84(65)	27(25)	4(4)	151(120)
[Ne V] 14.3	MIRI	4(4)	28(28)	21(21)	20(20)	15(15)	0(0)	0(0)	0(0)	0(0)	0(0)	0(0)	87(87)
	SMI	0(0)	11(11)	7(7)	7(7)	4(4)	5(5)	4(4)	0(0)	0(0)	0(0)	0(0)	39(39)
	SAFARI	0(0)	0(0)	0(0)	0(0)	0(0)	0(0)	0(0)	8(8)	6(6)	3(3)	1(1)	17(17)
[Ne III] 15.5	MIRI	8(4)	276(80)	222(80)	233(108)	164(83)	0(0)	0(0)	0(0)	0(0)	0(0)	0(0)	903(355)
	SMI	0(0)	147(46)	101(40)	103(47)	77(36)	77(49)	38(29)	0(0)	0(0)	0(0)	0(0)	544(248)
	SAFARI	0(0)	0(0)	0(0)	0(0)	0(0)	0(0)	34(27)	41(31)	59(48)	22(21)	5(5)	161(132)
[S III] 18.7	MIRI	2(1)	302(87)	184(69)	0(0)	0(0)	0(0)	0(0)	0(0)	0(0)	0(0)	0(0)	489(157)
	SMI	2(1)	135(43)	60(26)	48(21)	37(15)	0(0)	0(0)	0(0)	0(0)	0(0)	0(0)	281(106)
	SAFARI	0(0)	0(0)	0(0)	0(0)	0(0)	63(37)	23(16)	14(11)	13(10)	6(5)	1(1)	119(80)
[Ne V] 24.3	MIRI	1(1)	0(0)	0(0)	0(0)	0(0)	0(0)	0(0)	0(0)	0(0)	0(0)	0(0)	1(1)
	SMI	0.5(0.5)	28(28)	19(19)	0(0)	0(0)	0(0)	0(0)	0(0)	0(0)	0(0)	0(0)	47(47)
	SAFARI	0(0)	0(0)	27(27)	52(52)	26(26)	34(34)	21(21)	14(14)	15(15)	14(14)	2(2)	205(205)
[O IV] 25.9	MIRI	2(1)	0(0)	0(0)	0(0)	0(0)	0(0)	0(0)	0(0)	0(0)	0(0)	0(0)	2(1)
	SMI	2(1)	116(78)	0(0)	0(0)	0(0)	0(0)	0(0)	0(0)	0(0)	0(0)	0(0)	116(78)
	SAFARI	0(0)	0(0)	172(125)	204(168)	107(89)	134(124)	76(73)	42(40)	55(53)	45(45)	7(7)	842(724)
[S III] 33.5	MIRI	0(0)	0(0)	0(0)	0(0)	0(0)	0(0)	0(0)	0(0)	0(0)	0(0)	0(0)	0(0)
	SMI	3(1)	0(0)	0(0)	0(0)	0(0)	0(0)	0(0)	0(0)	0(0)	0(0)	0(0)	3(1)
	SAFARI	0(0)	647(180)	690(210)	680(336)	408(243)	556(401)	280(230)	75(56)	154(130)	52(49)	7(7)	3550(1841)
[Si II] 34.8	MIRI	0(0)	0(0)	0(0)	0(0)	0(0)	0(0)	0(0)	0(0)	0(0)	0(0)	0(0)	0(0)
	SMI	2(1)	0(0)	0(0)	0(0)	0(0)	0(0)	0(0)	0(0)	0(0)	0(0)	0(0)	2(1)
	SAFARI	1(0)	408(113)	402(133)	407(185)	272(141)	308(200)	140(107)	54(39)	80(62)	25(24)	3(3)	2100(1007)

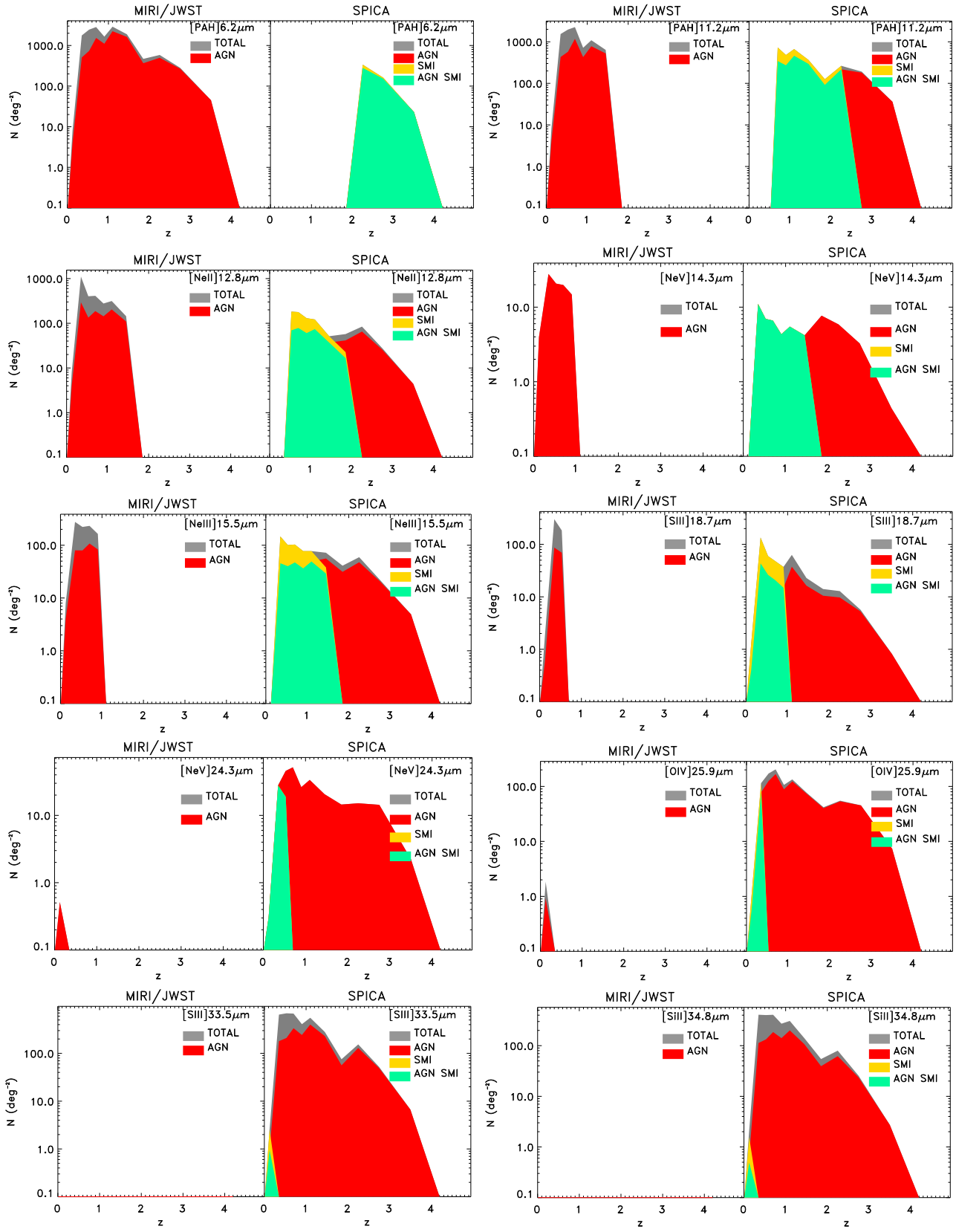

Figure 13. Redshift distribution (per unit area) of sources with fluxes of the different mid-IR lines larger than the MIRI-*JWST* sensitivities (5σ, 10 000 s; left) and the *SPICA* ones (5σ, 10 000 s; right), as expected based on the method described in this work. The total (e.g. AGN+galaxies) number of sources per unit area (for *SPICA* it is the number detectable by both SMI and SAFARI instruments) is shown as grey filled histogram, while the AGN contribution is shown in red. The yellow and green histograms highlight the SMI total and AGN contribution, respectively.

no variation with the AGN contribution for lines produced by SF. On the contrary, the normalization of the relation between the SF produced lines and the AGN luminosity increases with decreasing AGN fraction, while it shows no variation with the amount of AGN relative contribution for AGN signature lines.

(vi) These local line versus AGN/SF luminosity relations are then used, together with the recent *Herschel* galaxy LF and evolution results, to obtain IR line LFs up to high redshifts, in order to estimate for how many SF galaxies and AGN we expect to detect and measure the mid-/far-IR lines at different redshifts and luminosities with the forthcoming/planned future IR space missions (e.g. *JWST*, *SPICA*).

Since the nuclear properties are likely to be more correlated than those averaged over the whole galaxy size, the investigation of eventual relation between the nuclear AGN activity and the circumnuclear SF (rather than the global SF) would shed more light on the AGN/host galaxy connection. Spatially resolved observations of the nuclei of these Seyfert galaxies in the near-/mid-IR would be a natural extension of this work.

ACKNOWLEDGEMENTS

We thank an anonymous referee for helpful comments that improved the paper significantly. We would also like to thank Gianni Zamorani for his valuable help on the statistical tests and results. CG acknowledges financial contribution from the contracts ASI-INAF I00507/1 and I005110. This research has made use of the NASA/IPAC Extragalactic Database (NED, which is operated by the Jet Propulsion Laboratory, California Institute of Technology, under contract with the National Aeronautics and Space Administration), and of the SIMBAD database and the VizieR catalogue access tool (both operated at CDS, Strasbourg, France).

REFERENCES

Alonso-Herrero A. et al., 2014, MNRAS, 443, 2766
Armus L. et al., 2007, ApJ, 656, 148
Asmus D., Hönig S. F., Gandhi P., Smette A., Duschl W. J., 2014, MNRAS, 439, 1648
Baldwin J. A., Phillips M. M., Terlevich R., 1981, PASP, 93, 5
Barcons X., Franceschini A., de Zotti G., Danese L., Miyaji T., 1995, ApJ, 455, 480
Bernard-Salas J. et al., 2009, ApJS, 184, 230
Berta S. et al., 2013, A&A, 551, A100
Bonato M. et al., 2014a, MNRAS, 438, 2547
Bonato M. et al., 2014b, MNRAS, 444, 3446
Brightman M., Nandra K., 2011a, MNRAS, 413, 1206
Brightman M., Nandra K., 2011b, MNRAS, 414, 3084
Bruzual G., Charlot S., 2003, MNRAS, 344, 1000
Buchanan C. L., Gallimore J. F., O'Dea C. P., Baum S. A., Axon D. J., Robinson A., Elitzur M., Elvis M., 2006, AJ, 132, 401
Burgarella D. et al., 2013, A&A, 554, A70
Castro A. et al., 2014, PASJ, 66, 110
da Cunha E., Charlot S., Elbaz D., 2008, MNRAS, 388, 1595
Delvecchio I. et al., 2014, MNRAS, 439, 2736
Feltre A., Hatziminaoglou E., Fritz J., Franceschini A., 2012, MNRAS, 426, 120
Fritz J., Franceschini A., Hatziminaoglou E., 2006, MNRAS, 366, 767
Gandhi P., Horst H., Smette A., Hönig S., Comastri A., Gilli R., Vignali C., Duschl W., 2009, A&A, 502, 457
Gardner J. P. et al., 2006, Space Sci. Rev., 123, 485
Genzel R., Cesarsky C. J., 2000, ARA&A, 38, 761
Genzel R. et al., 1998, ApJ, 498, 579
Graciá-Carpio J. et al., 2011, ApJ, 728, L7
Granato G. L., Danese L., 1994, MNRAS, 268, 235
Groves B. A., Dopita M. A., Sutherland R. S., 2004, ApJS, 153, 9
Gruppioni C. et al., 2013, MNRAS, 432, 23
Gruppioni C. et al., 2015, MNRAS, 451, 3419
Hanami H. et al., 2012, PASJ, 64, 70
Harrison C. M. et al., 2012, ApJ, 760, L15
Harrison F. A. et al., 2013, ApJ, 770, 103
Hatziminaoglou E., Fritz J., Jarrett T. H., 2009, MNRAS, 399, 1206
Hewitt A., Burbidge G., 1991, ApJS, 75, 297
Hönig S. F., Kishimoto M., 2010, A&A, 523, A27
Hönig S. F., Leipski C., Antonucci R., Haas M., 2011, ApJ, 736, 26
Hopkins P. F., Richards G. T., Hernquist L., 2007, ApJ, 654, 731
Kataza H. et al., 2015, J. Astron. Instrum., 4, 50001
Kennicutt R. C., Jr, 1998, ARA&A, 36, 189
Kormendy J., Ho L. C., 2013, ARA&A, 51, 511
Luhman M. L., Satyapal S., Fischer J., Wolfire M. G., Sturm E., Dudley C. C., Lutz D., Genzel R., 2003, ApJ, 594, 758
Lutz D. et al., 2008, ApJ, 684, 853
Macklin J. T., 1982, MNRAS, 199, 1119
Madau P., Dickinson M., 2014, ARA&A, 52, 415
Malhotra S. et al., 2001, ApJ, 561, 766
Mullaney J. R., Alexander D. M., Goulding A. D., Hickox R. C., 2011, MNRAS, 414, 1082
Nakagawa T., Matsuhara H., Kawakatsu Y., 2012, in Clampin M. C., Fazio G. G., MacEwen H. A. Oschmann J. M., Jr, eds, Proc. SPIE Conf. Ser. Vol. 8442, Space Telescopes and Instrumentation 2012: Optical, Infrared, and Millimeter Wave. SPIE, Bellingham, p. 84420O
Nenkova M., Sirocky M. M., Nikutta R., Ivezić Ž., Elitzur M., 2008, ApJ, 685, 160
Netzer H., 2009, MNRAS, 399, 1907
Netzer H., 2015, ARA&A, 53, 365
Netzer H. et al., 2007, ApJ, 666, 806
Ochsenbein F., Bauer P., Marcout J., 2000, A&AS, 143, 23
Page M. J. et al., 2012, Nature, 485, 213
Panuzzo P., Bressan A., Granato G. L., Silva L., Danese L., 2003, A&A, 409, 99
Pereira-Santaella M., Diamond-Stanic A. M., Alonso-Herrero A., Rieke G. H., 2010, ApJ, 725, 2270
Pereira-Santaella M. et al., 2013, ApJ, 768, 55
Pier E. A., Krolik J. H., 1992, ApJ, 401, 99
Pozzi F. et al., 2010, A&A, 517, A11
Roelfsema P. et al., 2014, in Oschmann J. M., Jr, Clampin M. C., Fazio G. G., MacEwen H. A., eds, Proc. SPIE Conf. Ser. Vol 9143, Space Telescopes and Instrumentation 2014: Optical, Infrared, and Millimeter Wave. SPIE, Bellingham, p. 91431K
Rosario D. J. et al., 2012, A&A, 545, A45
Rubin R. H., Simpson J. P., Lord S. D., Colgan S. W. J., Erickson E. F., Haas M. R., 1994, ApJ, 420, 772
Rush B., Malkan M. A., Spinoglio L., 1993, ApJS, 89, 1 (RMS)
Rush B., Malkan M. A., Fink H. H., Voges W., 1996, ApJ, 471, 190
Schweitzer M. et al., 2006, ApJ, 649, 79
Shankar F., Weinberg D. H., Miralda-Escudé J., 2009, ApJ, 690, 20
Shao L. et al., 2010, A&A, 518, L26
Smith J. D. T. et al., 2007a, PASP, 119, 1133
Smith J. D. T. et al., 2007b, ApJ, 656, 770
Spinoglio L., Malkan M. A., 1989, ApJ, 342, 83
Spinoglio L., Malkan M. A., 1992, ApJ, 399, 504
Spinoglio L., Dasyra K. M., Franceschini A., Gruppioni C., Valiante E., Isaak K., 2012, ApJ, 745, 171
Spinoglio L., Pereira-Santaella M., Dasyra K. M., Calzoletti L., Malkan M. A., Tommasin S., Busquet G., 2015, ApJ, 799, 21
Stalevski M., Fritz J., Baes M., Nakos T., Popović L. Č., 2012, MNRAS, 420, 2756
Sturm E. et al., 2010, A&A, 518, L36
Tommasin S., Spinoglio L., Malkan M. A., Smith H., González-Alfonso E., Charmandaris V., 2008, ApJ, 676, 836
Tommasin S., Spinoglio L., Malkan M. A., Fazio G., 2010, ApJ, 709, 1257

Veilleux S. et al., 2009, ApJS, 182, 628
Veron-Cetty M.-P., Veron P., 1991, Eur. South. Obs. Sci. Rep., 10, 1
Wenger M. et al., 2000, A&AS, 143, 9
Wright G. S. et al., 2010, in Oschmann J. M., Jr, Clampin M. C., MacEwen H. A., eds, Proc. SPIE Conf. Ser. Vol. 7731, Space Telescopes and Instrumentation 2010: Optical, Infrared, and Millimeter Wave. SPIE, Bellingham, p. 77310E
Wu Y., Charmandaris V., Huang J., Spinoglio L., Tommasin S., 2009, ApJ, 701, 658

APPENDIX A: PHOTOMETRIC DATA

The photometric data for our 12MGS subsample of 76 sources with *Spitzer*-IRS spectra have been collected from NED, Vizier and Simbad public databases in fixed bands. Here, for the first time a 'homogenized' photometric catalogue is put together for this sample, with derived total fluxes (corrected for aperture and magnitude zero-point). In Tables A1 and A2 data from UV to *Spitzer*-IRAC bands and from 12 μm to 3 mm are presented, respectively.

Table A1. 12 MGS optical to mid-IR photometry.

Name	Flux (in mJy) at λ (in μm)																
	0.35	0.37	0.45	0.47	0.55	0.62	0.69	0.77	0.88	0.94	1.25	1.64	2.17	3.6	4.5	5.8	8.0
3C 120	...	...	2.2	...	3.6	...	8.1	...	...	...	32.4	44.7	44.7	...	...	...	...
3C 234	0.1	...	0.2	0.2	0.5	0.7	...	0.8	...	...	2.0	3.5	5.3	...	16.0	...	...
3C 273	10.4	...	25.4	23.1	27.4	25.8	...	32.2	...	...	42.7	42.7	100.0	...	...	...	...
3C 445	...	...	0.7	...	...	...	1.3	...	...	...	5.0	8.9	19.1	...	...	...	...
CGCG 381−051	...	...	3.2	...	2.6	...	...	...	...	...	12.3	15.9	14.5	9.8	8.4	15.6	110.4
ESO 012−G021	...	...	6.5	...	6.5	...	14.5	...	...	...	22.6	32.4	37.4	39.5	39.7	54.5	208.5
ESO 033−G002	...	...	6.0	...	5.5	...	15.2	...	...	...	48.3	69.4	65.0	48.8	60.1	78.8	140.3
ESO 141−G055	...	...	7.6	...	13.2	...	16.8	...	...	...	39.8	41.7	50.1	...	...	...	...
ESO 362−G018	...	...	12.6	...	17.0	...	27.9	...	...	...	57.9	71.4	65.2	35.7	31.8	57.1	140.3
IC 4329A	...	...	12.6	...	13.0	...	46.3	...	...	...	109.6	158.5	177.8	313.7	382.4	483.8	684.0
IC 5063	...	9.0	28.7	...	67.5	...	92.7	...	...	...	209.0	252.0	211.0	85.6	124.3	219.1	563.7
IRASF 01475−0740	...	...	0.8	...	2.1	...	1.9	...	...	...	7.0	10.1	9.7	13.1	19.9	42.1	87.7
IRASF 03450+0055	...	...	3.9	...	5.3	...	...	...	...	...	12.0	19.3	31.4	63.8	74.2	92.2	145.6
IRASF 04385−0828	...	...	2.2	...	6.0	...	...	...	...	...	16.2	26.3	37.2	64.9	109.3	175.7	355.7
IRASF 05189−2524	...	...	2.7	...	4.8	...	...	...	...	...	14.8	30.9	57.5	...	...	...	...
IRASF 07599+6508	5.4	...	8.0	6.4	...	6.7	7.9	8.0	...	7.0	10.0	20.9	32.4	...	...	...	...
IRASF 08572+3915	...	...	...	0.4	0.8	0.6	...	0.9	...	1.1	1.7	3.0	3.9	...	...	...	...
IRASF 13349+2438	1.8	...	...	2.2	3.8	6.3	...	5.3	...	7.7	14.1	26.9	52.5	...	...	...	...
IRASF 15480−0344	...	...	1.4	...	3.4	...	4.0	...	...	...	20.3	25.0	26.1	19.8	24.6	36.4	98.9
Izw 001	...	...	7.3	...	9.2	...	...	...	...	...	34.7	58.9	89.1	...	...	...	...
MCG−02−33−034	...	...	5.4	...	9.2	...	25.7	...	...	...	70.0	85.7	76.6	25.2	20.3	27.3	71.0
MCG−03−34−064	...	...	10.6	12.6	...	...	18.8	...	...	...	69.7	87.3	76.6	...	...	...	...
MCG−03−58−007	...	...	2.4	...	4.6	...	...	...	...	...	20.0	29.5	36.3	37.3	45.1	58.0	123.0
MCG−06−30−015	...	...	11.7	...	13.6	...	...	...	...	...	71.8	94.8	98.0	106.8	127.8	157.3	239.4
MCG+00−29−023	...	...	4.2	...	...	...	...	...	...	...	39.8	57.5	49.0	30.0	24.8	55.0	372.4
Mrk 0006	...	1.7	4.2	...	14.2	...	...	...	...	...	59.4	83.9	100.0	92.2	101.5	104.9	142.9
Mrk 0009	...	...	5.2	...	6.8	...	...	...	...	...	21.9	33.1	46.8	...	...	...	...
Mrk 0079	1.4	...	5.4	5.7	7.4	16.1	...	38.0	...	50.6	39.8	57.5	64.6	90.5	108.3	146.1	243.8
Mrk 0231	3.0	...	5.7	5.6	11.0	11.9	...	23.2	...	21.7	49.0	107.2	186.2	...	...	...	...
Mrk 0273	1.1	...	2.3	4.1	4.1	7.3	...	10.7	...	14.1	19.6	60.3	61.7	...	...	...	...
Mrk 0335	...	2.1	8.9	...	10.9	...	16.5	...	15.4	...	33.1	55.0	95.5	92.6	110.8	127.7	176.0
Mrk 0463	...	2.2	3.0	...	7.8	...	10.3	...	...	...	21.7	35.1	62.0	115.0	156.0	...	412.0
Mrk 0509	...	...	19.3	...	21.4	...	...	...	...	...	91.2	107.2	128.8	...	...	...	...
Mrk 0704	1.9	...	5.0	4.6	7.9	8.9	...	8.3	...	15.5	20.9	32.4	41.7	81.8	107.3	132.0	237.2
Mrk 0897	...	...	2.9	...	4.7	...	...	...	...	...	50.1	72.4	60.3	27.6	25.0	26.6	78.5
Mrk 1239	1.7	...	4.3	4.6	6.6	9.0	...	10.8	...	14.7	22.9	44.7	85.1	233.6	277.0	344.1	500.1
NGC 0034	...	...	9.3	...	14.8	...	20.6	...	42.9	...	51.1	67.1	62.3	42.5	36.2	92.2	590.3
NGC 0262	...	4.4	11.7	19.0	16.9	28.7	...	...	...	...	89.1	104.7	100.0	55.0	74.2	98.3	179.9
NGC 0424	...	...	13.2	...	44.2	...	38.5	...	84.8	...	100.7	131.0	148.7	207.3	301.0	413.7	671.5
NGC 0513	3.0	...	18.4	11.1	16.5	22.4	...	31.8	...	41.3	66.2	83.3	72.2	37.7	29.8	37.4	190.1
NGC 0526A	...	...	5.3	...	6.8	...	14.3	...	19.9	...	28.2	34.7	33.1	70.6	83.7	99.2	137.7
NGC 0931	...	...	2.2	...	4.8	...	...	...	...	...	57.5	81.3	87.1	124.9	142.7	205.4	312.7
NGC 1056	...	...	20.0	...	41.8	...	48.9	...	152.0	...	140.0	181.0	150.0	55.5	33.6	58.7	404.6
NGC 1125	...	...	10.8	...	21.2	...	35.2	...	...	...	...	...	32.8	26.8	24.4	47.9	159.6
NGC 1194	1.4	3.5	6.1	9.8	...	25.3	...	40.4	...	57.6	68.2	79.7	73.6	54.0	79.9	137.0	232.8
NGC 1320	...	7.0	19.8	...	39.6	...	...	...	...	...	100.0	125.0	112.0	64.4	73.5	117.1	264.9
NGC 1365	...	116.0	345.0	...	...	512.0	...	...	...	...	507.0	546.0	516.0	360.2	327.0	603.5	3214.1
NGC 1566	...	145.9	354.2	...	484.8	...	714.5	...	904.5	...	1264.7	1339.1	1173.8	574.0	395.4	460.0	1350.0
NGC 2992	2.0	4.0	9.2	...	12.7	...	15.8	13.9	...	16.6	22.4	28.6	23.8	116.0	106.3	144.8	464.6
NGC 3079	...	44.9	102.1	...	171.2	...	...	...	...	...	389.0	512.9	407.4	269.0	177.0	444.0	3350.0

Table A1 – *continued*

Name	Flux (in mJy) at λ (in μm)																
	0.35	0.37	0.45	0.47	0.55	0.62	0.69	0.77	0.88	0.94	1.25	1.64	2.17	3.6	4.5	5.8	8.0
NGC 3516	···	···	23.8	···	41.5	···	···	···	···	···	246.6	274.7	262.5	120.4	117.6	142.1	220.3
NGC 4051	5.3	···	15.5	26.2	25.7	···	···	···	···	···	74.1	109.6	107.2	108.8	119.8	166.2	382.9
NGC 4151	13.8	···	56.6	44.3	96.7	82.4	···	134.2	···	240.3	245.5	263.0	239.9	302.4	386.0	520.8	997.8
NGC 4253	4.0	···	7.7	13.8	14.1	24.4	···	31.1	···	40.6	26.9	49.0	63.1	66.8	84.4	104.9	257.7
NGC 4388	9.1	···	···	···	···	···	···	···	34.6	···	40.9	51.1	41.9	85.6	82.1	164.7	408.4
NGC 4593	···	···	11.1	···	20.8	···	···	···	···	···	169.8	195.0	158.5	124.9	133.8	163.2	290.4
NGC 4602	···	···	43.4	···	···	···	41.1	···	52.0	···	58.9	75.9	61.7	136.2	84.6	122.4	433.8
NGC 5135	···	···	39.2	···	76.1	···	84.3	···	···	···	195.0	295.1	257.0	73.9	65.2	132.0	756.9
NGC 5256	···	···	8.9	···	16.2	···	···	···	···	···	44.2	56.3	52.5	23.6	17.8	43.3	346.0
NGC 5347	4.2	···	17.4	19.9	31.4	38.7	···	55.9	···	71.4	89.9	105.0	92.5	31.7	37.2	61.5	152.4
NGC 5506	5.0	···	···	25.2	···	57.0	···	76.8	···	115.2	208.0	299.0	354.0	437.1	568.3	732.3	1104.2
NGC 5548	4.3	···	8.0	···	12.2	32.5	···	42.7	···	54.6	76.0	98.9	106.0	57.5	66.3	96.4	210.1
NGC 5953	9.6	···	21.5	36.5	39.6	61.0	···	83.2	···	109.0	131.0	161.0	135.0	62.6	36.2	95.7	736.3
NGC 5995	···	···	5.8	···	12.6	···	18.6	···	···	···	43.7	69.2	72.4	110.8	129.0	163.2	375.9
NGC 6810	···	···	48.9	···	122.9	···	179.5	···	···	···	83.0	79.3	89.4	155.8	97.0	148.8	1025.8
NGC 6860	···	···	14.0	···	14.6	···	48.1	···	···	···	92.5	118.8	116.9	66.8	75.6	107.8	183.3
NGC 6890	···	12.5	31.7	···	51.7	···	72.4	···	···	···	147.0	177.0	151.0	44.5	37.2	52.6	185.0
NGC 7130	···	···	31.5	···	···	···	72.7	···	···	···	115.0	141.0	125.0	47.5	39.0	78.1	558.5
NGC 7213	···	51.7	168.0	···	326.0	···	482.0	···	···	···	973.0	1120.0	942.0	340.0	270.0	270.0	340.0
NGC 7469	···	17.4	26.6	···	43.8	···	···	···	···	···	117.5	166.0	154.9	150.2	150.9	270.8	1188.7
NGC 7496	···	···	72.0	···	···	···	143.9	···	172.3	···	169.0	196.0	156.0	28.3	21.0	47.5	272.3
NGC 7603	3.8	···	5.4	13.9	9.4	24.2	···	28.0	···	51.4	354.8	501.2	416.9	143.4	156.5	178.9	298.6
NGC 7674	···	5.5	11.4	···	19.3	···	···	···	···	···	51.2	64.6	68.4	71.2	94.3	147.5	443.7
TOLOLO 1238−364	···	···	26.4	···	···	···	61.7	···	···	···	64.6	100.0	109.6	50.6	50.4	89.7	416.0
UGC 05101	0.5	···	3.5	···	···	5.8	···	8.5	···	12.0	16.4	25.1	33.0	80.0	160.0	206.0	340.0
UGC 07064	2.7	···	5.0	9.6	9.4	18.0	···	24.9	···	32.3	50.5	60.2	55.8	28.6	24.4	32.3	144.2

Table A2. 12 MGS mid-IR to mm photometry.

Name	Flux (in Jy) at λ (in μm)																			
	12	25	60	100	120	150	170	180	200	250	350	450	500	800	850	870	1100	1300	2000	3000
3C 120	0.43	0.67	1.55	4.82	4.00	5.10	9.90	···	···	···	···	···	···	1.00	1.82	···	1.50	···	1.40	1.80
3C 234	0.10	0.26	0.31	0.26	···	···	···	0.80	1.09	···	···	···	···	···	2.27	···	12.00	···	15.00	16.50
3C 273	0.55	0.89	2.06	2.89	1.49	1.09	1.10	0.80	0.79	···	···	···	···	7.00	8.00	···	10.00	···	15.00	16.50
3C 445	0.21	0.26	0.31	0.60	···	0.56	···	···	0.49	···	···	···	···	···	···	···	···	···	···	···
CGCG 381−051	0.16	0.51	1.75	2.76	···	···	1.82	···	···	···	···	···	···	···	···	···	···	···	···	···
ESO 012−G021	0.22	0.19	1.51	3.22	···	2.21	1.81	1.14	0.92	···	···	···	···	···	···	···	···	···	···	···
ESO 033−G002	0.24	0.47	0.82	1.84	···	···	···	···	···	···	···	···	···	···	···	···	···	···	···	···
ESO 141−G055	0.28	0.46	0.47	1.48	···	···	···	···	···	···	···	···	···	···	···	···	···	···	···	···
ESO 362−G018	0.23	0.57	1.28	2.34	2.54	1.86	···	0.86	0.55	···	···	···	···	···	···	···	···	···	···	···
IC 4329A	1.11	2.26	2.15	2.31	···	1.87	···	···	1.20	···	···	···	···	···	···	···	···	···	···	···
IC 5063	1.15	3.95	5.79	4.41	4.97	4.13	···	3.10	2.26	···	···	···	···	···	···	···	···	···	···	···
IRASF 01475−0740	0.32	0.84	1.10	1.05	···	···	···	···	···	···	···	···	···	···	···	···	···	···	···	···
IRASF 03450+0055	0.29	0.39	0.87	···	···	1.03	···	···	0.68	···	···	···	···	···	···	···	···	···	···	···
IRASF 04385−0828	0.59	1.70	2.91	3.55	···	···	···	···	···	···	···	···	···	···	···	···	···	···	···	···
IRASF 05189−2524	0.71	3.41	13.27	11.90	10.60	7.00	···	3.20	2.90	1.94	0.72	···	0.23	···	···	···	···	···	···	···
IRASF 07599+6508	0.33	0.54	1.75	1.47	···	···	···	···	···	···	···	···	···	···	···	···	···	···	···	···
IRASF 08572+3915	0.32	1.87	7.33	4.98	···	···	···	···	···	···	···	···	···	···	0.02	···	···	···	···	···
IRASF 13349+2438	0.61	0.72	0.85	0.90	···	···	0.35	···	···	···	···	···	···	···	···	···	···	···	···	···
IRASF 15480−0344	0.24	0.72	1.09	4.05	···	···	···	···	···	···	···	···	···	···	···	···	···	···	···	···
Izw 001	0.47	1.17	2.24	2.87	2.57	1.89	1.60	1.16	0.92	···	···	···	···	···	···	···	···	···	···	···
MCG−02−33−034	0.17	0.37	1.16	2.22	···	···	···	···	···	···	···	···	···	···	···	···	···	···	···	···
MCG−03−34−064	0.95	2.88	6.22	6.37	6.40	4.40	···	3.60	2.30	···	···	···	···	···	···	···	···	···	···	···
MCG−03−58−007	0.28	0.89	2.60	3.66	···	···	···	···	···	···	···	···	···	···	···	···	···	···	···	···
MCG−06−30−015	0.33	0.97	1.09	1.10	···	1.06	···	···	0.40	···	···	···	···	···	···	···	···	···	···	···
MCG+00−29−023	0.33	0.73	5.22	9.65	···	···	···	···	···	···	···	0.57	···	···	0.08	···	···	···	···	···
Mrk 0006	0.26	0.73	3.50	···	···	5.00	···	···	···	···	···	···	···	···	···	···	···	···	···	···
Mrk 0009	0.23	0.39	0.76	0.98	···	0.74	···	0.36	0.23	···	···	···	···	···	···	···	···	···	···	···
Mrk 0079	0.36	0.73	1.55	2.35	2.74	2.04	1.88	1.12	0.85	···	···	···	···	···	···	···	···	···	···	···
Mrk 0231	1.87	8.66	32.00	30.30	24.30	16.10	20.80	9.75	6.88	···	···	···	···	···	···	···	···	···	···	···
Mrk 0273	0.22	2.30	22.80	22.20	23.60	16.95	8.30	7.48	5.75	···	1.34	0.71	···	···	0.06	···	···	0.01	···	···

Table A2 *– continued*

Name	Flux (in Jy) at λ (in μm)																			
	12	25	60	100	120	150	170	180	200	250	350	450	500	800	850	870	1100	1300	2000	3000
Mrk 0335	0.27	0.45	0.35	0.57	...	...	...	...	...	...	...	...	...	...	...	...	...	...	...	...
Mrk 0463	0.47	1.49	2.21	1.99	2.26	0.99	...	...	0.45	...	...	0.11	...	...	...	...	...	...	...	...
Mrk 0509	0.30	0.73	1.39	1.36	...	...	1.00	...	...	...	...	...	...	...	...	...	...	...	...	...
Mrk 0704	0.42	0.60	0.36	0.45	...	...	...	...	...	...	...	...	...	...	...	...	...	...	...	...
Mrk 0897	0.37	0.86	2.97	5.59	...	...	...	...	...	...	...	...	...	...	...	...	...	...	...	...
Mrk 1239	0.76	1.21	1.68	2.42	...	...	...	...	...	...	...	...	...	...	...	...	...	...	...	...
NGC 0034	0.40	2.51	16.84	17.61	17.20	10.60	8.50	5.40	...	3.28	1.15	...	0.35	...	...	...	...	...	...	...
NGC 0262	0.49	1.02	1.43	1.43	2.24	2.28	1.89	1.29	1.14	...	...	...	...	...	...	...	...	...	...	0.36
NGC 0424	1.22	1.76	2.00	1.74	...	...	1.16	...	...	...	...	...	...	...	...	...	...	...	...	...
NGC 0513	0.17	0.28	1.93	4.05	...	...	...	...	...	...	...	...	...	...	...	...	...	...	...	...
NGC 0526A	0.23	0.48	2.31	4.08	...	...	...	...	...	...	...	...	...	...	...	...	...	...	...	...
NGC 0931	0.62	1.42	2.80	5.66	...	5.54	5.25	3.72	2.88	...	...	...	...	...	...	...	...	...	...	...
NGC 1056	0.36	0.48	5.49	10.22	...	...	...	...	...	2.15	1.09	...	0.24	...	...	...	...	...	...	...
NGC 1125	0.32	1.00	3.71	4.04	...	...	...	...	...	...	...	...	...	...	...	...	...	...	...	...
NGC 1194	0.28	0.85	0.92	0.71	...	...	...	...	...	...	...	...	...	...	...	...	...	...	...	...
NGC 1320	0.31	1.32	2.21	2.82	3.70	2.58	...	1.44	1.06	...	...	...	...	...	...	...	...	...	...	...
NGC 1365	4.42	13.07	84.20	185.40	217.00	194.00	167.00	103.00	85.20	145.80	62.30	24.70	...	...	...	...	...	...	...	...
NGC 1566	1.91	3.02	22.50	58.10	...	95.26	...	...	...	51.50	22.20	9.10	...	...	...	...	...	...	...	...
NGC 2992	0.51	1.58	10.78	17.05	...	...	...	...	...	...	...	...	...	...	...	...	...	...	...	...
NGC 3079	2.60	3.65	50.70	105.17	...	...	91.30	...	...	...	10.70	3.70	...	0.80	...	...	...	0.50	...	...
NGC 3516	0.39	0.96	2.09	2.73	...	...	...	...	...	...	...	...	...	...	...	...	...	...	...	...
NGC 4051	0.86	2.20	10.53	24.93	...	...	...	...	...	1.49	0.78	...	0.34	...	...	...	...	...	...	...
NGC 4151	1.95	4.87	6.46	8.50	4.40	...	3.00	...	...	0.59	0.31	...	0.13	...	...	...	...	...	...	...
NGC 4253	0.35	1.47	3.89	4.20	...	...	...	...	...	...	...	...	...	...	...	...	...	...	...	...
NGC 4388	1.03	3.72	10.27	17.15	...	...	19.51	...	...	2.39	1.33	...	0.61	...	0.29	...	...	0.01	...	...
NGC 4593	0.47	0.96	3.43	6.26	...	8.10	...	...	4.70	...	...	...	...	...	...	...	...	...	...	...
NGC 4602	0.54	0.56	4.75	12.60	...	...	...	...	...	...	...	...	...	...	...	...	...	...	...	...
NGC 5135	0.58	2.39	16.60	31.18	...	...	...	...	...	9.20	3.85	...	1.37	...	...	...	...	...	...	...
NGC 5256	0.30	1.13	7.27	10.07	...	...	8.73	...	...	...	...	...	...	...	0.08	...	...	...	...	...
NGC 5347	0.30	0.96	1.43	2.64	...	...	...	...	...	...	...	...	...	...	...	...	...	...	...	...
NGC 5506	1.25	4.24	8.44	9.24	...	...	...	...	...	...	...	...	...	...	...	...	...	...	...	...
NGC 5548	0.43	0.81	1.07	1.61	...	...	...	...	...	...	...	...	...	...	...	...	...	...	...	...
NGC 5953	0.82	1.67	11.85	20.47	17.00	17.20	15.50	...	...	...	...	...	...	...	0.18	...	...	...	...	...
NGC 5995	0.41	1.45	4.09	7.06	...	...	...	...	...	...	...	...	...	...	...	...	...	...	...	...
NGC 6810	1.33	3.61	18.90	33.30	...	29.80	...	16.90	14.00	...	...	...	...	...	...	...	...	...	...	...
NGC 6860	0.25	0.31	0.96	2.19	...	...	...	...	...	...	...	...	...	...	...	...	...	...	...	...
NGC 6890	0.36	0.80	4.01	8.26	11.70	8.80	...	5.10	4.36	...	...	...	...	...	...	...	...	...	...	...
NGC 7130	0.64	2.15	16.85	26.96	28.90	21.90	16.90	10.80	7.29	6.49	2.92	...	1.04	...	...	...	...	...	...	...
NGC 7213	0.65	0.81	2.70	9.15	...	13.62	...	...	6.60	...	...	...	...	...	...	...	...	...	...	...
NGC 7469	1.58	6.04	28.57	35.83	33.00	26.00	29.00	...	...	7.82	3.07	...	0.99	...	0.19	...	...	...	...	...
NGC 7496	0.62	2.00	10.21	16.59	20.80	16.20	13.90	8.89	6.25	...	...	...	...	...	...	...	...	...	...	...
NGC 7603	0.40	0.24	1.25	2.00	...	...	...	...	...	...	...	...	...	...	...	...	...	...	...	...
NGC 7674	0.64	1.79	5.64	8.46	9.38	7.65	6.02	3.67	2.78	...	...	...	...	...	0.11	...	...	...	...	...
TOLOLO 1238−364	0.66	2.63	9.08	14.03	...	...	7.42	4.60	3.62	...	...	...	...	...	...	...	...	...	...	...
UGC 05101	0.35	1.11	11.64	20.52	...	...	...	...	...	5.83	2.35	...	0.79	0.14	...	0.04	0.07	0.01	...	...
UGC 07064	0.17	0.38	2.75	5.57	...	...	...	...	...	...	...	...	...	...	...	...	...	...	...	...

This paper has been typeset from a TEX/LATEX file prepared by the author.